INORGANIC CHEMISTRY
FRONTIERS

RESEARCH ARTICLE

View Article Online
View Journal | View Issue

Cite this: *Inorg. Chem. Front.*, 2024, **11**, 2319

Development of In–Cu binary oxide catalysts for hydrogenating CO_2 *via* thermocatalytic and electrocatalytic routes†

Marco Pietro Mezzapesa, [a] Fabio Salomone, [a] Hilmar Guzmán, [a] Federica Zammillo,[a] Roberto Millini,[d] Letizia Bua,[c] Gianluigi Marra,[b] Alessandra Tacca,[b] Rosamaria Marrazzo, [b] Nunzio Russo,[a] Raffaele Pirone,[a] Simelys Hernández *[a,e] and Samir Bensaid*[a]

Carbon dioxide (CO_2) hydrogenation to obtain valuable chemicals and fuels *via* thermocatalysis or electrocatalysis is a promising and sustainable method for CO_2 utilization. Here, binary In–Cu oxide co-precipitated materials were investigated to evaluate the catalytic performance in the mentioned conversion processes. The In-rich binary material exhibits remarkable selectivity (>60%) to methanol along with high activity for CO_2 conversion (>2%) at 21 bar and 300 °C, achieving a productivity of about 265 mg_{MeOH} h^{-1} $g_{In_2O_3}^{-1}$, which is almost 3 times higher than that of the bare In_2O_3 catalyst. CO_2-temperature programmed desorption revealed that the basicity of the In-rich catalyst remains constant between the calcined and spent samples, so the capacity to adsorb CO_2 does not vary when the catalyst is exposed to the reaction atmosphere. Such a catalyst was demonstrated to be active for formate production in the electrochemical process as the main product. *Ex situ* characterization after testing proved that the In_2O_3 phase was the active site of methanol synthesis during CO_2 hydrogenation at high temperatures and pressures. In contrast, depending on the cell configuration, different indium interfaces were stabilized at the electrocatalyst surface under ambient conditions. It is envisioned that the co-presence of In^0, In_2O_3, and $In(OH)_3$ phases increases the local amount of *CO intermediates, promoting the formation of more reduced products, such as ethanol and 2-propanol, through the *CO dimerization reaction in the electrochemical process. These findings highlight the potential of nonreducible hydroxides as promoters in the electrochemical CO_2 reduction process.

Received 4th December 2023,
Accepted 20th February 2024

DOI: 10.1039/d3qi02499g

rsc.li/frontiers-inorganic

Introduction

Nowadays, greenhouse gases present a serious problem. In particular, CO_2 is a greenhouse gas emitted by many human activities as a waste product (*e.g.* automobiles, chemical industry, home heating, *etc.*). Carbon Capture and Storage (CCS) or Carbon Capture and Utilization (CCU) are possible solutions to reduce environmental impact, such as by capturing CO_2 from flue gas. In particular, CCU provides the possibility of transforming it into high-value products (*e.g.*, methanol, gasoline, and olefins). Among the possible products, methanol has specific relevance; in fact, it can be used as a solvent, fuel additive or chemical building block and in different processes, for example:

- Methanol Steam Reforming (MSR[1–3]) is useful for transporting hydrogen and using it as a clean energy source;
- Gasoline production (methanol-to-gasoline[4–7]);
- Olefin production (methanol-to-olefins[4,5,8–12]).

Methanol production is a known industrial catalytic process. Currently, methanol is produced by passing a CO:CO_2:H_2 mixture over a copper-based catalyst;[13–15] the main reactions involved in the methanol synthesis process are CO_2 hydrogenation, Reverse Water Gas Shift (RWGS) reaction, CO hydrogenation, and CO_2 and CO methanation that are reported in eqn (1), (2), (3), (4) and (5), respectively.[4,16,17]

$$CO_2 + 3H_2 \rightleftharpoons CH_3OH + H_2O \quad \Delta_R H^\circ = -49.5\ \text{kJ mol}^{-1} \quad (1)$$

$$CO_2 + H_2 \rightleftharpoons CO + H_2O \quad \Delta_R H^\circ = +41.5\ \text{kJ mol}^{-1} \quad (2)$$

[a]*Department of Applied Science and Technology (DISAT), Politecnico di Torino, Corso Duca degli Abruzzi 24, 10129 Turin, Italy. E-mail: samir.bensaid@polito.it, simelys.hernandez@polito.it*
[b]*Eni S.p.A., DE-R&D, Via Giacomo Fauser 4, 28100 Novara, Italy*
[c]*Eni S.p.A., R&D, Via Giacomo Fauser 4, 28100 Novara, Italy*
[d]*Eni S.p.A., DOW R&D, Via Felice Maritano 26, 20097 San Donato Milanese, Milan, Italy*
[e]*Istituto Italiano di Tecnologia (IIT), Via Livorno 60, 10144 Turin, Italy*
† Electronic supplementary information (ESI) available. See DOI: https://doi.org/10.1039/d3qi02499g

$$CO + 2H_2 \rightleftharpoons CH_3OH \quad \Delta_R H^\circ = -91.0 \text{ kJ mol}^{-1} \quad (3)$$

$$CO_2 + 4H_2 \rightleftharpoons CH_4 + 2H_2O \quad \Delta_R H^\circ = -165 \text{ kJ mol}^{-1} \quad (4)$$

$$CO + 3H_2 \rightleftharpoons CH_4 + H_2O \quad \Delta_R H^\circ = -206 \text{ kJ mol}^{-1} \quad (5)$$

Thus, the methanol synthesis process involves a series of by-products, the main ones being CO (2) and CH_4 (thermodynamically favored products). For executing this process industrially, the catalyst $Cu/ZnO/Al_2O_3$ (CZA) is used. This catalyst works at pressures between 50 and 100 bar and temperatures in the range 240–280 °C. Under these conditions, CZA enables high CO_2 conversion but poor methanol selectivity.[4,18,19] With CZA, copper adsorbs CO_2 and helps its conversion to CO for subsequent hydrogenation to methanol; otherwise, ZnO is needed to store hydrogen and react with CO and CO_2 *via* reactions (1)–(5).[13–15]

In the literature, researchers have proposed different catalysts for producing methanol with higher performance. In particular, In_2O_3 catalysts have shown good methanol selectivity and CO_2 conversion. Chou *et al.*[18] have shown a series of different catalysts with their performance, and among these catalysts are those based on indium (In_2O_3). The indium oxide catalyst presents a better performance than CZA in terms of methanol selectivity and yield. Martin *et al.*[20] have tested CZA and In_2O_3 under the same conditions and have compared their performance. Under their reaction conditions (300 °C, 50 bar, $H_2/CO_2 = 4:1$ and GHSV equal to 16 000 h^{-1}), In_2O_3 has a methanol productivity of 0.20 $g_{MeOH}\ h^{-1}\ g_{cat}^{-1}$ and CZA has a productivity of 0.15 $g_{MeOH}\ h^{-1}\ g_{cat}^{-1}$. There is an even more significant difference in terms of methanol selectivity: for In_2O_3, it is nearly 100%, and for CZA it is about 16%. In addition, Martin *et al.*[20] observed a monotonic increase in productivity *vs.* temperature (200–300 °C) for In_2O_3 and an opposite trend for CZA. This difference could be related to the fact that the RWGS reaction is slower in In_2O_3 than in CZA, because In_2O_3 does not catalyze reaction (2). Thereafter, In_2O_3 inhibits CO formation. Furthermore, CO is a substance capable of activating In_2O_3; this is because it reduces the indium oxide and increases the oxygen vacancies.[20,21] Indeed, oxygen vacancies play a central role in the In_2O_3 catalytic methanol synthesis mechanism, as it involves their structural features to adsorb and activate CO_2.[22] Like each catalyst, the performance of In_2O_3 can be further enhanced by adding the right support or promoters. Martin *et al.*[23] have shown that zirconia (ZrO_2) induces the formation of oxygen vacancies on the surface of In_2O_3 and inhibits CO formation, so it is possible to have higher conversion without losing selectivity. Frei *et al.*[24] have studied the effect of palladium (Pd) on In_2O_3 catalysis; they observed that atomically dispersed Pd inhibits RWGS (2) and improves both the stability and activity of In_2O_3. In addition, they have recently investigated the effect of dispersion of different metals on the surface of In_2O_3 for enhancing methanol productivity.[25]

The aforementioned catalysts for the production of methanol have been studied to exploit the thermocatalytic (TC) process of CO_2 conversion. Among the different technologies, TC processes are currently suitable for wide market size and large scale of production with a high technological readiness level. However, focusing attention on emerging technologies and future scenarios, electrocatalytic (EC) processes may become suitable and very promising under certain circumstances and they could have similar environmental impact.[16] For these reasons, this study investigates the applicability of our catalysts for both TC and EC processes. Thus, the literature review on these kinds of catalysts for EC applications reported hereunder will help in understanding the state-of-the-art on these catalysts.

Among the different materials studied for CO_2 electroreduction (CO_2R), indium metal has been proposed as a suitable electrocatalyst due to its intrinsic high overpotential towards the HER and interesting formate selectivity.[26] Nonetheless, several studies have reported that materials based on indium suffer from low activity. Moreover, the poor stability of these catalysts has been also shown.[27] The rational design of catalysts can enable a significant improvement of the metrics needed for the practical application of CO_2R. Among the strategies, indium-based catalysts with different morphologies have been developed to enhance their selectivity. Xia and coworkers[28] synthesized a needle-like porous electrode that displayed a lower onset potential compared to the indium foil electrode. The novel nanostructured catalyst also enabled a faradaic efficiency (FE) toward formate of 86%, with a current density of 5.8 mA cm^{-2} at −0.86 V *vs.* RHE. Another strategy discussed in the literature is the incorporation of a second metal into In nanoparticles to form bimetallic materials. Either alloys or heterostructures can be formed, resulting in electronic interactions or synergistic effects at the interfacial regions. Either way the catalyst selectivity shifts to carbon monoxide from formate. Rasul *et al.*[29] designed a surface Cu–In alloy by electrochemically depositing In on a rough Cu layer which showed a stable FE of 85% for CO for 7 h. In the work performed by Luo and colleagues, a thin layer of metallic In was deposited on Cu nanowires, achieving a FE_{CO} of about 93% at −0.6 to −0.8 V *vs.* RHE with a remarkable stability of 60 hours.[30] According to density functional theory (DFT) calculations, that selectivity is attributed to the enhanced adsorption strength of *COOH and the destabilization of the *H adsorption on the Cu–In interfaces. On the other hand, monodisperse core–shell Cu/In_2O_3 nanoparticles were synthesized in another work to boost syngas formation.[31] Herein, a wide range of H_2/CO ratios was obtained by varying the In_2O_3 shell thickness. The mechanistic discussion revealed that the compression strain and Cu dopant in the shell both promoted CO selectivity. By combining electrochemical measurements with *ex situ* characterization techniques, surface $In(OH)_3$ sites have been suggested by Larrazábal *et al.* as the active species that play a crucial role in selective CO formation.[32] Furthermore, the work performed by Zhu *et al.* demonstrated that, by changing the metal ratio of Cu/In, the catalyst selectivity shifts from CO (core–shell structure) to HCOOH (well-mixed structure). DFT calculations helped correlate the structure-sensitive

binding strength of the *COOH and *OCHO intermediates with the catalytic performance.[33]

In this work, the catalytic activities and deactivation phenomena of bimetallic In/Cu catalysts are assessed. In particular, the main focus is on the effect of Cu on In_2O_3 activity and the achievement of a better-performing catalyst with respect to In_2O_3 and Cu alone. Shi *et al.*[34,35] have recently studied In–Cu binary oxide catalysts for methanol synthesis from CO_2. They have tested this kind of catalyst in TC and observed the formation of In–Cu alloys. As a result, the alloy increased the methanol yield and catalyst stability.[35] Moreover, they observed that the formation of the $Cu_{11}In_9$ alloy enhances the performance more than the presence of the Cu_7In_3 alloy.[34] However, they have not investigated the formation of these alloys in the EC CO_2 conversion process and they have compared samples with relatively high amounts of Cu and In atoms (*i.e.*, from Cu/In = 1/3 to Cu/In = 3/1), without studying the effect of doping.

The catalysts reported here were synthesized using the gel–oxalate coprecipitation technique that allowed us to obtain samples with a wide specific surface area and small crystallites.[36–38] Binary oxide catalysts ($In_xCu_{100-x}O_y$) with five different In/Cu atomic ratios were prepared, characterized, and tested, for the first time, for both the thermochemical and electrochemical conversion of CO_2 and H_2 to added-value products. The chosen atomic ratios were 0, 10, 50, 90, and 100 to explore the whole range of possible compositions. Characterization was also performed on each sample to evaluate its chemical, physical, and morphological characteristics. For the thermocatalytic tests, characterization was performed on fresh and spent catalysts. In a recent work, we found that Cu–Zn-based catalysts operate with some similarities in the reaction mechanisms of TC and EC CO_2 conversion.[17] Thus, the aim of this work is to deeply investigate the catalytic performances of In–Cu-based catalysts in these two processes and find eventual synergies that can be exploited to develop novel electrocatalysts inspired by the thermocatalysts for the sustainable production of chemicals and fuels.

Methodology

Catalyst synthesis

As done by Shi *et al.*,[34,35] the catalysts were synthesized using the co-precipitation technique. In our work, oxalates were co-precipitated from metal nitrates (indium and copper). Each sample was prepared by dissolving an appropriate amount of salts ($In(NO_3)_3{\cdot}xH_2O$ and $Cu(NO_3)_2{\cdot}3H_2O$) in ethanol to obtain a 0.1 mol L^{-1} solution of metallic cations. On the other hand, 1 mol L^{-1} oxalic acid solution in ethanol was prepared with an excess of 20% of oxalic acid with respect to the stoichiometric amount. The solutions were prepared under ambient conditions with vigorous stirring. Then, the oxalic acid solution was added dropwise to the nitrate solution and the suspension was kept under stirring for 2 h. After the mixing time, the suspension was centrifuged (4000 rpm for 15 min) for collecting the oxalate gel from the bottom of the test tube. This gel was dried in an oven (70 °C for 16 h). Finally, the dried product was crushed and then calcined to produce oxides (50 °C ramp rate, +10 °C min^{-1} until 360 °C for 4 h). To perform the catalytic tests, each powder was pelletized under a loading of 2.65 kN, then the pellets were crushed and sieved between 250 μm and 500 μm to obtain the catalytic particles.

The tested catalysts have the following formula: $In_xCu_{100-x}O_y$, where x is the atomic fraction of indium. The synthesized catalysts are denoted as Cu_{100}, $In_{10}Cu_{90}$, $In_{50}Cu_{50}$, $In_{90}Cu_{10}$, and In_{100}. Indeed, the used formula does not report oxygen, but it is important to remember that they are oxides. Also, in the article the $Cu_\alpha In_\beta$ type formula represents indium–copper alloys.

Characterization analyses

Both fresh and spent catalysts were analyzed using several characterization techniques. First of all, the metallic composition was investigated by inductively coupled plasma mass spectrometry (ICP-MS), the specific surface area and the porosity of each catalyst were determined by N_2 physisorption at 77 K and the structural features were evaluated by X-ray diffraction (XRD) and Raman spectroscopy. The reducibility of each sample was determined with temperature programmed reduction (H_2-TPR), while the basicity was studied with temperature programmed desorption (CO_2-TPD). Moreover, carbonaceous species deposited on the spent catalysts were quantified by means of temperature programmed combustion (TPC). Lastly, we performed scanning electron microscopy (SEM) and transmission electron microscopy (TEM).

Inductively coupled plasma mass spectrometry (ICP-MS). Each calcined catalyst (~30 mg) was mineralized in 30 mL of 0.5 M H_2SO_4 and 0.25 M L-ascorbic acid aqueous solution; it was kept under stirring at room temperature overnight. After that, each sample was diluted with Milli-Q water to obtain 100 mL of concentrated solution. Subsequently, each concentrated solution was diluted using deionized Milli-Q water to obtain a concentration of each metal cation within the calibration range (0.1–2 mg L^{-1}). Finally, each sample was analyzed using an inductively coupled plasma mass spectrometer (iCAP Q ICP-MS, Thermo Fisher Scientific).[37]

N_2 physisorption measurements. Moisture and adsorbed species were removed from the catalytic powders by pre-treating them with flowing nitrogen for 2 h at 200 °C in a Micromeritics FlowPrep 060. The N_2 physisorption measurements were carried out in a Micromeritics Tristar ASAP II 3020 analyzer. The specific surface area was evaluated using the Brunauer–Emmett–Teller (BET) method and the porosimetry analysis was performed according to the Barrett–Joyner–Halenda (BJH) procedure.[37]

X-ray diffraction measurements. XRD measurements were performed on both fresh calcined and spent samples under ambient conditions with a Philips X'Pert PW3040 diffractometer at 40 kV and 40 mA, using Ni β-filtered Cu-Kα radiation characterized by a wavelength (λ) equal to 1.5406 Å. The XRD pattern acquisition range was for 2θ angles 20°–90° (scan step

size: 0.013°; time per step: 0.3 s). The average crystallite was evaluated through Scherrer's equation.

Raman spectroscopy. The samples were analyzed using a Horiba LabRam HR 800 confocal microscope, with 473 nm laser excitation. The Raman spectra were collected in back-scattering, under a 50× objective, 600 lines per mm grating and CCD detector.

X-ray photoelectron spectroscopy. The surface of the catalysts was analyzed by means of *ex situ* XPS employing a PHI Versa Probe equipment, using an X-ray spot diameter of 100 μm and a take-off angle of 45°. The XPS spectra were collected employing a band-pass energy of 187.85 eV for survey scans and a band pass energy of 23.50 eV for high resolution (HR) scans.

Temperature-programmed measurements. H_2-TPR and CO_2-TPD analysis were performed in a Thermoquest TPD/R/O 1100 analyser equipped with a thermal conductivity detector (TCD).

On the one hand, to perform the H_2-TPR analyses, a suitable mass of the catalyst (~20 mg) was firstly pre-treated under flowing He (40 cm^3 min^{-1}) at 300 °C (heating rate: +10 °C min^{-1}) for 30 min. Then, the sample was cooled down to 50 °C under He flow. The H_2-TPR analysis was performed by feeding a stream of 5 mol% H_2/Ar (20 cm^3 min^{-1}) from 50 °C to 900 °C (+10 °C min^{-1}) and holding it at 900 °C for 30 min.

On the other hand, to perform the CO_2-TPD analyses, a certain amount of each catalyst (~80 mg) was pre-treated under He flow (40 cm^3 min^{-1}) at 300 °C for 30 min and cooled down to 50 °C. Afterwards, the sample was saturated with flowing pure CO_2 (40 cm^3 min^{-1}) at 50 °C for 60 min. After that, the reactor was purged using He flow (40 cm^3 min^{-1}) at 50 °C for 45 min. The CO_2-TPD analysis was performed under flowing He (20 cm^3 min^{-1}) from 50 °C to 900 °C (+10 °C min^{-1}) and holding it at 900 °C for 30 min.

The TPC analyses were performed in a U-tube quartz reactor containing 100 mg of spent catalyst (bed height: ~5 mm). The reactor was fed with 100 cm^3 min^{-1} of 5 mol% O_2/N_2 mixture without any pre-treatment. The oven was heated up to 800 °C with a heating rate of +10 °C min^{-1}. Then, the oven was kept at 800 °C for 10 min. The concentrations of CO_2 and CO at the outlet of the reactor were measured using an ABB Uras 14 gas analyzer, while the concentration of O_2 was measured using an Emerson X-Stream analyzer.

SEM and TEM measurements. High resolution micrographs were collected by scanning electron microscopy using a FE-SEM JEOL JSM 7600F with an accelerating voltage of 15 kV and using secondary electron signals. All the samples were analyzed as made, without undergoing any kind of metallization procedure, and after grinding the powders were fixed on conducting carbon tape.

High-resolution TEM (HRTEM) characterization was performed by using a JEOL (Akishima, Tokyo, Japan) JEM 2010 UHR, equipped with a LaB_6 electron gun operating at 200 kV. All digital micrographs were acquired using an UltraScan 1000 camera, and the images were processed by a Gatan digital micrograph (Pleasanton, CA, USA). Specimens for HRTEM analysis were sonicated in 2-propanol and then transferred, as a suspension, to a copper grid covered with a holey carbon film. Micrographs were taken after solvent evaporation, spanning over the whole region of the sample to achieve a truly representative statistical mapping of the investigated material.

Thermocatalytic activity test

A stainless-steel fixed bed reactor (i.d. 8 mm) was used to test the catalytic activity of the synthesized catalysts. The reactor was heated with an insulated oven that enabled it to reach and maintain the desired temperature. The reactor outlet gases were analyzed with a gas-chromatograph (GC – Agilent Technologies 7890B GC system) equipped with a thermal conductivity detector (TCD) and a flame ionization detector (FID). Fig. S1† shows the plant configuration used for the thermocatalytic tests.

Each sample (1.0 g of catalytic particles) was pre-treated under flowing N_2 (60 NL h^{-1}) at 2 bar from room temperature to 300 °C (heating rate: 10 °C min^{-1}) and holding it at 300 °C for 1 h. After that, thermocatalytic tests were sequentially performed in the same reactor. The stability test was carried out feeding the reaction mixture (20 NL h^{-1} g_{cat}^{-1} with a $H_2/CO_2/N_2$ molar ratio of 15/5/1) at 21 bar and 275 °C for 20 h. After stabilization, activity tests were carried out varying the temperature from 200 °C to 300 °C under the same reaction gas flowrate and pressure.

CO_2 conversion (ζ_{CO_2}), methanol selectivity (σ_{CH_3OH}) and methanol yield (η_{CH_3OH}) were evaluated for each test according to eqn (6)–(8), respectively.

$$\zeta_{CO_2} = \frac{\dot{n}_{CO_2,in} - \dot{n}_{CO_2,out}}{\dot{n}_{CO_2,in}} = \frac{\sum_{i \neq CO_2} \left(N_{C,i} \cdot \dot{n}_{i,out}\right)}{\dot{n}_{CO_2,in}} \quad (6)$$

$$\sigma_{CH_3OH} = \frac{\dot{n}_{CH_3OH,out}}{\dot{n}_{CO_2,in} - \dot{n}_{CO_2,out}} = \frac{\dot{n}_{CH_3OH,out}}{\sum_{i=1}^{N_P} \left(N_{C,i} \cdot \dot{n}_{i,out}\right)} \quad (7)$$

$$\eta_{CH_3OH} = \zeta_{CO_2} \cdot \sigma_{CH_3OH} \quad (8)$$

where $\dot{n}_{CO_2,in}$ and $\dot{n}_{CO_2,out}$ are the inlet and outlet molar flowrates (mol s^{-1}) of CO_2, $\dot{n}_{i,in}$ represents the outlet molar flowrate (mol s^{-1}) of the i-th species, N_P is the number of products, $N_{C,i}$ is the number of carbon atoms of the i-th species and $\dot{n}_{CH_3OH,out}$ is the outlet molar flowrate (mol s^{-1}) of methanol.

Deactivation study

Based on the data obtained from the stability test, the deactivation phenomenon was studied. This methodology shows the equation used for modelling the deactivation kinetics. The hypothesis refers to the fluid dynamics of the gas flow through the catalytic bed located in the reactor. (a) sintering phenomenon is the predominant deactivation mechanism; (b) the reaction kinetic order is equal to 1; (c) the deactivation kinetic order is equal to 1 or 2; (d) the reactor fluid-dynamic was approximated with plug constant flow.[39] The equations for studying deactivation were obtained by putting the following

equations into a system: the reaction rate expression (9) and deactivation kinetics (10).

$$r'_A = -k' \cdot {C_A}^n \cdot a \quad (9)$$

$$\frac{da}{dt} = -k_d \cdot {C_A}^m \cdot a^d \quad (10)$$

where r'_A (mol m^{-3} h^{-1}) is the reaction rate of the key reactant with deactivation, C_A (mol m^{-3}) is the concentration of the key component, a (dimensionless) is the activity (defined as r'_A/r_A, with r_A as the reaction rate without deactivation), k' ((mol m^{-3})$^{1-n}$ h^{-1}) is the kinetic constant of reaction, k_d ((mol m^{-3})$^{1-m}$ h^{-1}) is the kinetic constant of deactivation, t (s) is the time on stream, n (dimensionless) is the reaction order for the key reagent, m (dimensionless) is the reaction order for the key reagent in the deactivation kinetics, and d (dimensionless) is the deactivation order. In the solving procedure, τ' is defined as the reciprocal of gas hourly space velocity. So, τ' is equal for each catalyst and equal to 0.05 kg_{cat} h Nm^{-3} (catalyst mass/volumetric inlet flowrate). Furthermore, ζ_A is the key-reagent conversion; and CO_2 was chosen as the key-reagent for the calculation.

Therefore, eqn (11) and (12) can be obtained by linearizing the expressions of the variation of the CO_2 conversion with time by assuming first-order and second-order deactivation kinetics, respectively. Both equations were obtained by assuming first-order reaction kinetics and the independence of the deactivation kinetic with respect to the concentration of the gas species.[37]

$$\ln\left[\ln\left(\frac{1}{1-\zeta_A}\right)\right] = \ln(\tau' \cdot k') - k_d \cdot t \quad (11)$$

$$\ln^{-1}\left(\frac{1}{1-\zeta_A}\right) = \frac{1}{k' \cdot \tau'} + \frac{k_d}{k' \cdot \tau'} \cdot t \quad (12)$$

Kinetic study. Considering that the activation test was performed at different temperatures, it is possible to construct the Arrhenius plot. With the Arrhenius plot, it is possible to evaluate the apparent activation energy (E'_a) and pre-exponential factors (k') for CO_2 hydrogenation and methanol and CO synthesis.[37] The reaction rate and Arrhenius equation could be combined in eqn (13). In this equation, R_i (mol$_i$ kg_{cat}^{-1} h^{-1}) is the reaction rate, ρ_{cat} (kg_{cat} m^{-3}) is the catalytic bed density, $k'_{\infty,i}$ ((mol$_i$ m^{-3})$^{1-n}$ h^{-1}) is the pre-exponential factor, $E_{a,i}$ (kJ mol^{-1}) is the apparent activation energy, C_i (mol$_i$ m^{-3}) is the concentration of the i-th compound, n (dimensionless) is the order of reaction with respect to the i-th species likely seen in eqn (9), and $k^*_{\infty,i}$ (mol$_i$ kg_{cat}^{-1} h^{-1}) is the apparent pre-exponential factor.

$$R_i = r_i \cdot {\rho_{cat}}^{-1} = k'_{\infty,i} \cdot e^{-\frac{E_{a,i}}{R \cdot T}} \cdot {C_i}^n \cdot {\rho_{cat}}^{-1} = k^*_{\infty,i} \cdot e^{-\frac{E_{a,i}}{R \cdot T}} \quad (13)$$

The approximation adopted for eqn (9) is used in eqn (13). Then, eqn (13) is linearized in eqn (14),[37] to remove the dependence between the apparent activation energy and the apparent pre-exponential factor. For this reason, the value of the apparent activation energy is fixed, and the apparent pre-exponential factor is made explicit.

$$\ln(R_i) = \ln\left(k^*_{\infty,i}\right) - \frac{E_{a,i}}{R} \cdot \frac{1}{T} \quad (14)$$

Electrocatalytic set-up and tests

Gas diffusion electrode-based setup. A commercial micro flow cell from ElectroCell was employed to conduct continuous electrochemical experiments. The commercial cell comprises different layers, and depending on the stacking order of the layers, the pathways for gaseous and liquid streams can be defined. Fig. 1 shows that the gaseous CO_2 (green stream) flows through the standardized cut-out and crosses the 10 cm^2 geometrical area of the GDE to reach the active sites of the catalyst layer. Unreacted CO_2 and gaseous products cross the GDE, leaving the cell from the top exit (orange stream). Likewise, following the liquid electrolyte pathway (blue stream), the catholyte faces the electrocatalyst on one side while the membrane compartment on the other side. This latter compartment is constituted by two gaskets where the anion exchange membrane (AEM; FAA-3 from Fumasep) is inserted. Furthermore, moving to the anodic section, where the leak-free reference electrode (RE) is positioned, the anolyte faces the membrane compartment on one side and an iridium mixed metal oxide (Ir-MMO) anode plate on the other.

The catholyte and anolyte, 1 M KOH aqueous solutions, were recirculated with a flux rate of 26.5 mL min^{-1}. A mass flow controller was used to keep the gas flow rate constant at 20 NmL min^{-1}. The online gas product analysis was carried out by using a micro gas chromatograph (Agilent 990 Micro GC, equipped with Molsieve 5Å and Pora PLOT U capillary columns). A multichannel potentiostat (BioLogic VSP-300) was used for the electrochemical measurements.

Preparation of the gas diffusion electrodes. The electrode manufacturing method consisted of two main steps: preparation of a catalytic ink and subsequent deposition onto porous carbon paper (Toray 060) by an airbrushing process. In particular, the formulated ink was prepared by sequentially adding the catalyst powder, a carbon support (Vulcan XC 72R Carbon) to enhance the electron's conductivity and catalyst dispersion, an ionomer (Nafion) to bind the particles and ensure the ion pathways lie within the catalyst layer, and a

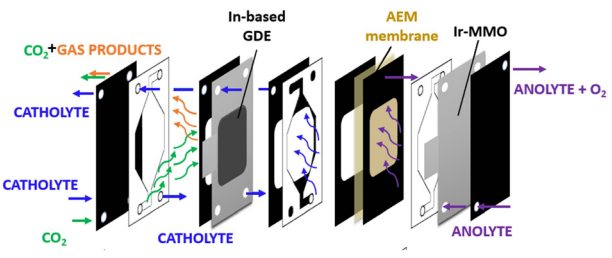

Fig. 1 Schematic view of an experimental setup involving a continuous flow cell in GDE configuration.

solvent (isopropyl alcohol) as the liquid carrier for ink deposition. Afterwards, the ink was coated onto a geometric area of 10 cm^2 to have a catalyst loading of 1.4 mg cm^{-2}, keeping the carbon paper on a heating plate at 120 °C to ensure solvent evaporation.

Electrode measurements. Each GDE was subjected to a pre-reduction process through galvanostatic treatment under −20 mA cm^{-2} for 40 minutes. Afterwards, cyclic voltammetry (CV) under N_2 and CO_2 environments was performed to evaluate the electrochemical behavior of the catalyst in the working solution and compare the activity under inert and reactive atmospheres. Then, the onset potential was estimated by linear sweep voltammetry (LSV) by scanning the potential up to −2.5 V *vs.* Ag/AgCl under continuous CO_2 flow. Finally, galvanostatic measurements (chronopotentiometry, CP) at −50 mA cm^{-2} were carried out and maintained constant for 2 h to evaluate the selectivity and stability of the investigated catalytic system.

Membrane electrode assembly setup. The GDEs were prepared as previously described. Then, the electrode was assembled using the commercial FAA-3 membrane by hot pressing at 120 °C under 35 bar for few minutes to form a membrane electrode assembly (MEA). The continuous electrochemical reduction of CO_2 was also carried out using the micro flow cell from ElectroCell. In this case, the MEA served as both a separator of the cathode and anode compartments, and a working electrode. Humidified CO_2 and 1 M KOH aqueous solution (as anolyte) were continuously fed to the different compartments, as shown in Fig. 2. The humid stream was obtained by sending the CO_2 flow through a closed water container heated at 80 °C as described in the GDE preparation section. The electrochemical characterization of the MEAs was assessed following the protocol detailed above.

Results and discussion

Characterization of the fresh calcined samples

Characterization of the calcined samples was mainly performed to study the synthesised product's features. First of all, ICP analysis was performed to verify the correct metal composition in the binary catalyst. In Table 1 In/(In + Cu) data from the ICP analysis are reported, confirming that the final powders have the desired composition. For all the samples a mesoporous structure was obtained. The pores size was evaluated by N_2 physisorption at 77 K and the results are reported in Table 1. Isotherms and pore distributions are reported in the ESI (Fig. S2 and S3†). Adsorption–desorption isotherms show the hysteresis phenomena confirming the mesoporosity of the powders. The shape of the hysteresis loop is associated with type IV isotherms. The hysteresis loops are like type H3; the only exception is $In_{10}Cu_{90}$, which is type H2. This indicates that each sample (except $In_{10}Cu_{90}$) contains an aggregate of plate-like particles. For $In_{10}Cu_{90}$ using the De Boer classification, this curve was type E so there are thin-bottle-shaped pores.[40–42] From the analysis of the physisorption of nitrogen at 77 K, the specific surface (SSA_{BET}) of the sample is also evaluated (shown in the Table 1). The $In_{10}Cu_{90}$ catalyst shows the highest specific surface, which could be associated to the lower crystallite sizes and pore sizes (d_P) than that of the other samples. In contrast, pure copper oxide (Cu_{100}) has a very low specific surface area as expected. On the other hand, In_{100} has a higher specific surface area than Cu_{100}. SSA_{BET} does not decrease much with an addition of 10% copper with respect to In_{100}.

Table 1 Characterization analysis results for fresh samples. The table includes results of ICP analysis and N_2 physisorption

Sample	$\frac{In}{In+Cu}$ at%	V_{BJH} $cm^3\ g^{-1}$	d_P nm	SSA_{BET} $m^2\ g^{-1}$
In_{100}	100	0.134	12.7	35.6
$In_{90}Cu_{10}$	89.1	0.147	17.3	30.0
$In_{50}Cu_{50}$	44.8	0.113	16.8	22.2
$In_{10}Cu_{90}$	7.8	0.156	7.8	54.0
Cu_{100}	0	0.019	33.8	2.1

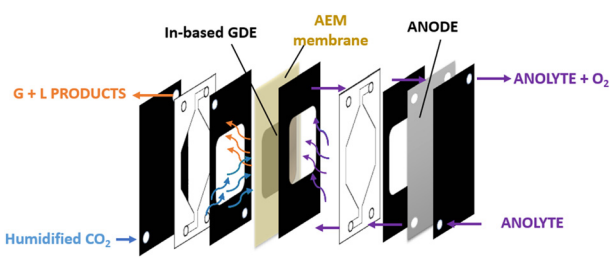

Fig. 2 Schematic view of a continuous flow cell in MEA configuration.

The diffractograms of the fresh calcined samples are reported in Fig. 3. The main crystalline oxide phases evidenced in the different catalysts are: In_2O_3, CuO (tenorite), and Cu_2O (cuprite). For the In_{100} catalyst, the In_2O_3 main peaks are located at 21.49°, 30.57°, 35.44°, 50.98°, and 60.60° (PDF 00-006-0416). The same In_2O_3 peaks are found in $In_{90}Cu_{10}$ and $In_{50}Cu_{50}$ diffractograms. In contrast, no peaks of In_2O_3 are detected in the $In_{10}Cu_{90}$ sample. This deficiency could be due to the low fraction of indium oxide in the catalyst. With respect to the Cu_{100} catalyst, the XRD diffractogram outlines the co-presence of CuO, Cu_2O and Cu (with the fractions shown in Table 2). In fact, the pattern shows the peaks at 32.42°, 35.51°, 38.71°, 48.81°, 61.58°, and 67.95° (PDF 00-048-1548) for CuO, the peaks at 29.57°, 36.43°, 42.31°, 61.39°, and 73.50° (PDF 00-005-0667) for Cu_2O and the peaks at 43.3° (PDF 00-004-0836) for Cu. The XRD diffractograms give another information: The Cu_{100} diffractogram presents the most intense peaks. Therefore, this higher intensity could be related to a larger particle size than in the other samples. No peaks of Cu_2O were found in the binary oxide catalysts, in contrast to the CuO peaks that are seen in all of them. The Raman spectra are consistent with the XRD data. In the Raman spectra of the Cu_{100} fresh sample (shown in Fig. S4 and S5†), two bands

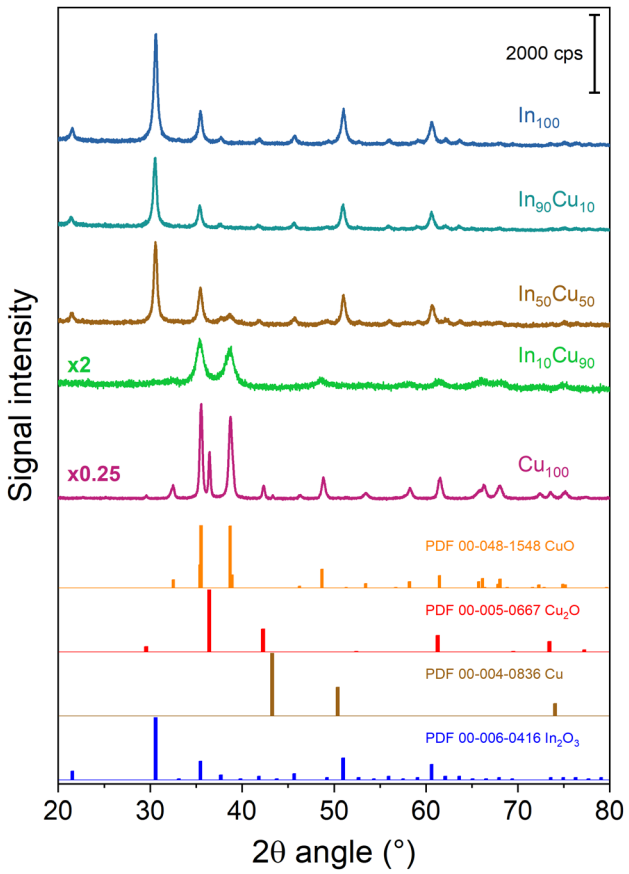

Fig. 3 XRD diffractograms of the fresh calcined samples. For the sake of clarity, a diffractogram with multiplicative values has the measured intensity multiplied by that factor.

located at 215 cm^{-1} and 138 cm^{-1} are related to the modes of Cu_2O, while two bands at 327 and 279 cm^{-1} are due to CuO.[43] On the other hand, the Raman bands of Cu_2O are not present in the spectra of $In_{90}Cu_{10}$ and $In_{10}Cu_{90}$ fresh samples. For all samples, the high full width at half maximum of the Raman bands suggests a small size of the crystallites. The size of the crystallites was calculated from the XRD diffractograms through Scherrer's equation. The crystallite dimensions obtained are reported in Table 2. In_2O_3 crystallites have a comparable dimension for each catalyst (≈24 nm). Instead, the CuO phase varies its dimension in different cases. The highest value of crystallite size is for Cu_{100}. For the binary oxide catalyst, the crystallite size decreased if Cu fraction increased.

The catalysts were characterized by the SEM technique and the images are shown in Fig. 4. In the binary samples, the two phases are not easily distinguished. In the figure it can be seen that the indium-based catalysts are more porous than the copper oxide ones. In particular, the $In_{10}Cu_{90}$ catalyst has a very sponge-like structure, in agreement with the high surface area of this sample. Moreover, an intimate contact between the In_2O_3 and CuO phase was confirmed from the TEM images (Fig. S6 and Table S1†).

Another important feature is the catalysts' reducibility. This property is evaluated for each sample by H_2-TPR analysis. Reducibility is an important characteristic as the catalyst will be exposed to a H_2-rich environment and high temperatures and pressures for the TC tests. In particular, it is important that CuO and Cu_2O are reduced to metallic copper (the active catalytic phase).

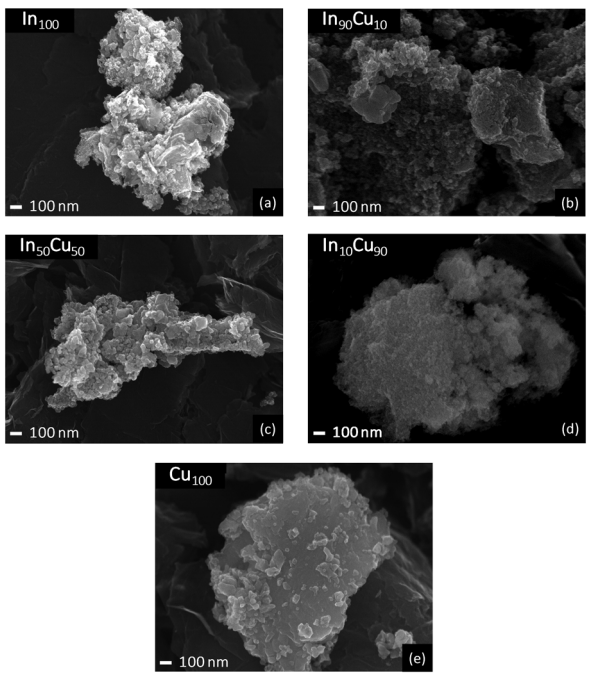

Fig. 4 SEM images for fresh catalysts (50k× magnification).

Table 2 Quantitative analysis of the phases detected by means of XRD of the fresh samples

	Phase fraction				Crystallite size (nm)			
Sample	In_2O_3	CuO	Cu_2O	Cu	In_2O_3	CuO	Cu_2O	Cu
In_{100}	100%	—	—	—	21.8	—	—	—
$In_{90}Cu_{10}$	100%	—	—	—	25.1	30.0	—	—
$In_{50}Cu_{50}$	56.4%	43.6%	—	—	23.9	13.0	—	—
$In_{10}Cu_{90}$	—	100%[a]	—	—	—	8.8	—	—
Cu_{100}		84.6%	14.4%	1.0%	—	32.6	58.9	115

[a] Other unidentified inorganic phases.

At the same time, In_2O_3 should not be reduced under the reaction conditions. H_2-TPR analysis confirms this behaviour, as shown in Fig. 5 and from the data reported in Table 3.

The reducibility of copper increases on decreasing the copper content in the samples. Indeed, Cu_{100} shows an asymmetric peak at 350 °C while $In_{90}Cu_{10}$ has a symmetric peak at 212 °C. The asymmetry of the Cu_{100} peak is attributed to the presence of Cu_2O. Finally, an increase in the reacted H_2 is observed as the fraction of indium present increases (In_{100} excluded).

Finally, the basicity of each catalyst was evaluated by CO_2-TPD.

Table 3 reports the integral results obtained from this analysis. For binary oxide catalysts, the Cu-rich catalysts show a higher amount of desorbed CO_2 which could be related to higher basicity. So, it is expected that the $In_{10}Cu_{90}$ catalyst will exhibit greater catalytic activity.

In conclusion, the most promising catalysts appear to be $In_{90}Cu_{10}$ and $In_{10}Cu_{90}$. $In_{10}Cu_{90}$ shows a high specific surface area and intimate contact (low crystallite size and microscopy results). $In_{90}Cu_{10}$ shows good specific surface area compared to Cu_{100} and H_2-TPR reports good copper distribution of In_2O_3 with small particles, which is confirmed by the lowest copper reduction temperature.

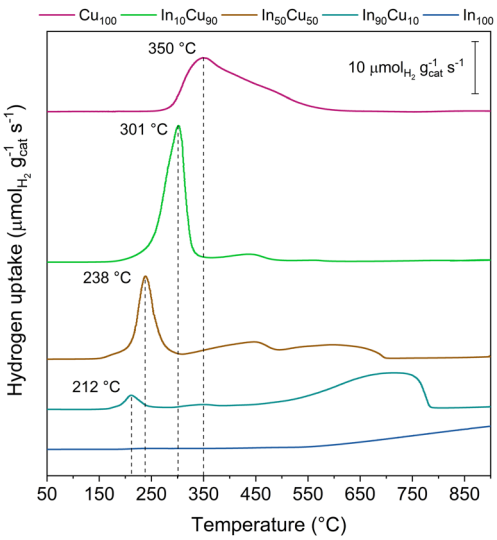

Fig. 5 H_2-TPR analysis plot results. The peaks assigned were related to CuO reduction. The other signal could be related to a Cu_2O reduction and a partial In_2O_3 reduction.

Table 3 Temperature programmed analysis integral results for the synthesized samples

Sample	H_2 uptake $\mu mol_{H_2}\ mg_{cat}^{-1}$	CO_2 desorbed $\mu mol_{CO_2}\ mg_{cat}^{-1}$
In_{100}	3.18	0.886
$In_{90}Cu_{10}$	11.75	0.459
$In_{50}Cu_{50}$	11.23	0.808
$In_{10}Cu_{90}$	10.28	1.723
Cu_{100}	9.66	—

Thermocatalytic results

This section shows the results of the thermo-catalytic tests on the catalysts. The thermo-catalytic results are preceded by the characterization of the spent catalysts. Then, the stability thermo-catalytic test and activity thermo-catalytic test are reported.

Characterization of the spent samples. Characterization analyses allow us to investigate the textural feature variations due to catalytic activities. First of all, physisorption of nitrogen at 77 K was conducted for examining the sintering phenomena. Table 4 reports the results of N_2 physisorption at 77 K for the spent catalysts. The main variation between fresh and spent samples is related to the reduction of SSA_{BET}. The SSA_{BET} reduction is similar between samples In_{100}, $In_{90}Cu_{10}$, and Cu_{100} and settles at about 50%. On the other hand, $In_{50}Cu_{50}$ and $In_{10}Cu_{90}$ show a very high decline in the specific surface areas due to the sintering phenomena.

Hence, Cu-rich binary oxide catalysts show low structural stability. Other interesting information comes from the XRD analysis of the spent catalysts. The XRD diffractograms obtained for these catalysts are shown in Fig. 6.

First of all, reduction of copper oxides (CuO, Cu_2O) is revealed in the Cu_{100} catalyst. Indeed, the peaks at 43.12°, 50.25°, and 73.93° are associated with metallic copper (PDF 00-004-0836). At the same time, In_2O_3 persists in its oxidation state (In_{100} sample). In fact, the In_{100} XRD diffractogram reveals the same peaks as those of the fresh catalyst (Fig. 3). These aspects of indium oxide are also true for the binary oxide catalysts, where the copper peaks are not always visible. Moreover, all binary oxide catalyst diffractograms reveal the formation of alloys. Starting from the spent $In_{90}Cu_{10}$ XRD diffractogram, there are peaks associated with In_2O_3 and the Cu_7In_3 alloy (at 29.5°, 34.3°, 41.7°, and 42.3°, PDF 03-065-2249). In the $In_{50}Cu_{50}$ spent catalyst, in addition to In_2O_3 peaks, the formation of $Cu_{11}In_9$ and Cu_9In_4 alloys is observed. In fact, the peaks at 29.4°, 32.9°, 41.4°, 42.07°, and 42.1° (PDF 03-065-4963) are associated with the $Cu_{11}In_9$ alloy and the peaks at 29.4°, 34.2°, 37.9°, 42.0°, 43.9°, 47.3°, 52.2°, 55.7°, 58.8°, 61.3°, 72.7°, 76.1°, and 77.5° (PDF 00-002-1178) are associated with the Cu_9In_4 alloy. For the $In_{10}Cu_{90}$ spent catalyst, three phases are observed: Cu with the same abovemen-

Table 4 N_2 physisorption analysis results for spent samples.

Sample	V_{BJH} $cm^3\ g^{-1}$	d_P nm	SSA_{BET} $m^2\ g^{-1}$	$\Delta_{\%}SSA_{BET}$[a] —
In_{100}	137.09	29.42	18.3 ± 0.1	48%
$In_{90}Cu_{10}$	137.93	29.93	15.1 ± 0.1	50%
$In_{50}Cu_{50}$	26.028	33.08	2.5 ± 0.1	89%
$In_{10}Cu_{90}$	7.902	11.87	1.7 ± 0.1	97%
Cu_{100}	2.065	16.36	1.2 ± 0.1	43%

[a] $\Delta_{\%}SSA_{BET} = (SSA_{BET,\ Fresh} - SSA_{BET,\ Spent})/SSA_{BET,\ Fresh}$.

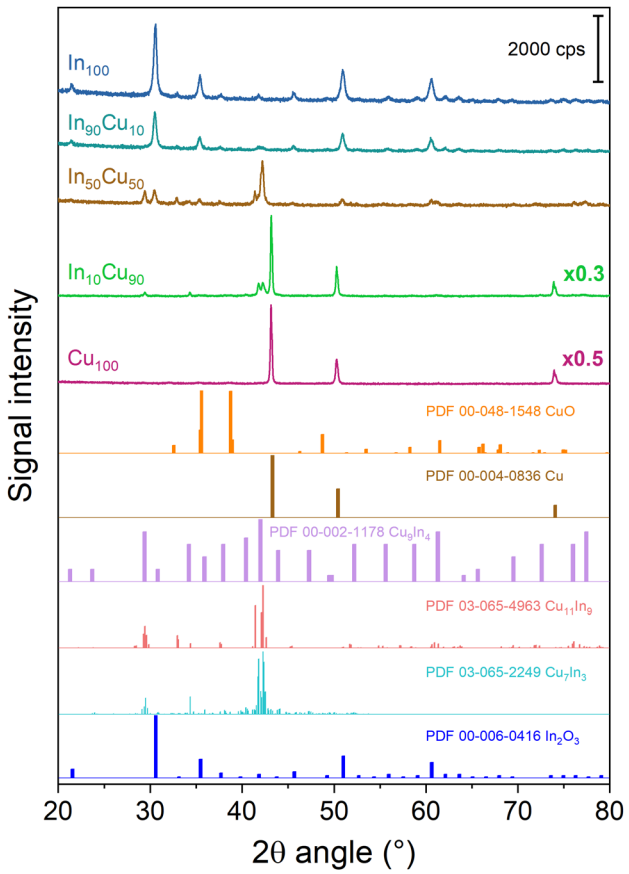

Fig. 6 XRD diffractograms of the spent TC samples. For the sake of clarity, a diffractogram with multiplicative values has the measured intensity multiplied by that factor.

tioned peaks, In_2O_3 with two peaks at 30.6° and 60.6° and the Cu_7In_3 alloy with the peaks at 29.5°, 34.3°, 41.7°, and 42.3° (PDF 03-065-2249). As mentioned previously, alloy formation is a phenomenon studied by Shi *et al.*[35,44] They have shown that the presence of In–Cu alloys enhances the activity and stability of the catalysts for the TC CO_2 conversion. Shi *et al.*[35] have shown that $Cu_{11}In_9$ is formed during the oxide reduction at 350 °C with pure H_2 (In : Cu = 2 : 1); under these conditions, an amount of In_2O_3 and all the CuO present in the catalyst were reduced. The presence of this alloy influences the Cu and In_2O_3 features leading to an increase of the H_2 adsorption over Cu (alloy) and of the CO_2 adsorption strength over the In_2O_3 at the interface with the alloy. Generally, this alloy shows thermal stability and an increase in methanol production. In a later work, Shi *et al.*[44] have shown that the post-reduction composition of the catalyst varies with the Cu : In molar ratio. Two alloys $Cu_{11}In_9$ and Cu_7In_3, were mainly observed, but the first one remains the best option (highest Cu dispersion and highest oxygen vacancy concentration). For obtaining only the $Cu_{11}In_9$ alloy, Shi *et al.*[45] found that the In : Cu molar ratio must be lower or equal to 2 : 1. In this work, $Cu_{11}In_9$ alloy formation was observed. According to the literature,[45] the $Cu_{11}In_9$ alloy could help the H_2 adsorption over Cu. At the same time, the $Cu_{11}In_9$–In_2O_3 interface could enhance the CO_2 adsorption over In_2O_3. Looking at the XRD diffractogram, another important information is obtained from the crystallite size (Table 5).

By comparing copper oxides' crystallite size with that of metallic copper, an increase in dimension in the spent catalysts is observed. Therefore, a sintering phenomenon due to reduction processes occurs. What was observed by XRD analysis is confirmed by Raman spectroscopy (Fig. S7–S11†). Raman spectroscopy for In_{100} and $In_{90}Cu_{10}$ did not reveal significant differences; at the same time, for Cu_{100} and $In_{10}Cu_{90}$ samples, a decrease of CuO content and an increase of Cu_2O content from fresh to spent catalysts were observed. The formation of Cu_2O could be ascribed to the aging process that reduced CuO. However, Raman spectroscopy was an *ex situ* measurement, so the superficial passivation of Cu was possibly not excluded. Moreover, for the $In_{10}Cu_{90}$ spent catalyst, the full width at half maximum of the CuO Raman bands decreased, confirming the effects of the sintering phenomena that occurred during the reaction. Analysis of the crystalline planes obtained by TEM (pictures are shown in Fig. S6 and Table S1†) highlights the formation of the Cu_7In_3 alloy in the $In_{90}Cu_{10}$ spent catalyst (see Table 5).

The SEM technique is applied again over the spent catalyst. Fig. 7 shows the pictures captured by the microscope. The SEM technique highlights the sintering phenomena due to high-temperature and reductive ambient conditions during the reaction. In fact, each image shows a reduction in the sponginess with more compact particles. In particular, spent Cu_{100} (Fig. 7(e)) shows very compact and bigger particles compared to other catalysts.

Temperature-programmed analyses (TPC, TPD) were performed over the spent catalysts. CO_2-TPD evaluates the basicity variation due to the reaction's ambient exposure. Table 6 reports the integral results for CO_2 desorbed over spent cata-

Table 5 Results of the XRD measurements carried out on the TC-spent catalysts

	Phase fraction (%)						Crystallite size (nm)					
Sample	In_2O_3	CuO	Cu	Cu_7In_3	$Cu_{11}In_9$	Cu_9In_4	In_2O_3	CuO	Cu	Cu_7In_3	$Cu_{11}In_9$	Cu_9In_4
In_{100}	100	—	—	—	—	—	32	—	—	—	—	—
$In_{90}Cu_{10}$	90.7	—	—	9.3	—	—	33	—	—	30	—	—
$In_{50}Cu_{50}$	18.6	—	—	—	54.9	26.5	36	—	—	—	140	20
$In_{10}Cu_{90}$	1.9	—	62.3	35.8	—	—	—	—	52	51	—	—
Cu_{100}	—	7.4	92.6	—	—	—	—	12	88	—	—	—

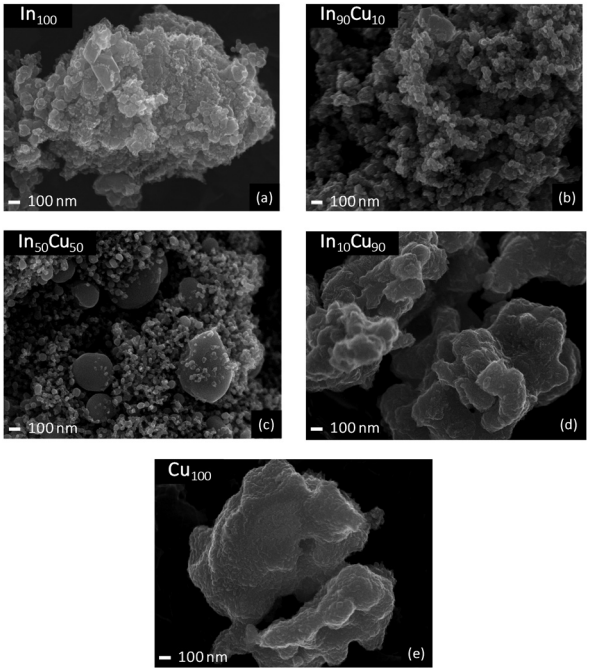

Fig. 7 SEM images of the TC spent catalysts: (a) 80k× magnification; (b–e) 50k× magnification.

Table 6 Temperature programmed analyses of the TC spent catalysts

Sample	Carbonaceous mass fraction %	CO_2 desorbed $\mu mol_{CO_2}\ mg_{cat}^{-1}$
In_{100}	0.39	4.054
$In_{90}Cu_{10}$	0.36	0.385
$In_{50}Cu_{50}$	0.05	0.084
$In_{10}Cu_{90}$	0.14	0.137
Cu_{100}	0.50	n.a.

lysts. The catalyst with the highest basicity is In_{100}, which quintuples the desorbed CO_2. For binary catalysts, a loss of the trend is observed. The In-rich catalyst has the highest basicity compared to the other binary catalysts. Then, TPC evaluated the carbonaceous substance deposited on the catalyst surface. Table 6 reports the carbonaceous mass fraction obtained from TPC analysis. The highest value was obtained for Cu_{100}. At the same time, In_{100} and $In_{90}Cu_{10}$ show a similar carbonaceous fraction. From these measurements, we can conclude that the deactivation occurs mainly by sintering with respect to the deposition of carbonaceous material. Finally, by comparing CO_2-TPD and TPC, it is observed that as the basicity of the catalyst increases, and there is a greater fraction of carbon deposited.

Thermocatalytic performance: stability test and deactivation. The first catalytic test performed was the 20 h stability test. This test evaluated the catalyst performance at 275 °C, 21 bar, under flowing 20 NL h^{-1} g_{cat}^{-1} of gas mixture $H_2/CO_2/N_2$ with a molar ratio of 15/5/1. Fig. 8 shows the results of catalytic performance obtained during this test, including the CO_2 conversion for each catalyst and the thermodynamic equilibrium. The thermodynamic equilibrium was only calculated for CO and methanol at 275 °C. CO_2 conversion appears with an initial rapid decrease followed by a slower conversion reduction phase. The highest CO_2 conversion is recorded by $In_{90}Cu_{10}$. On the other hand, $In_{10}Cu_{90}$ shows nil conversion. Finally, it is necessary to highlight how the $In_{50}Cu_{50}$ catalyst starts with almost nil conversion (0.8% *ca.*) and goes to zero in 20 h. Regarding the methanol selectivity, all the In-based catalysts report a higher value than Cu_{100}. $In_{90}Cu_{10}$ evinces the

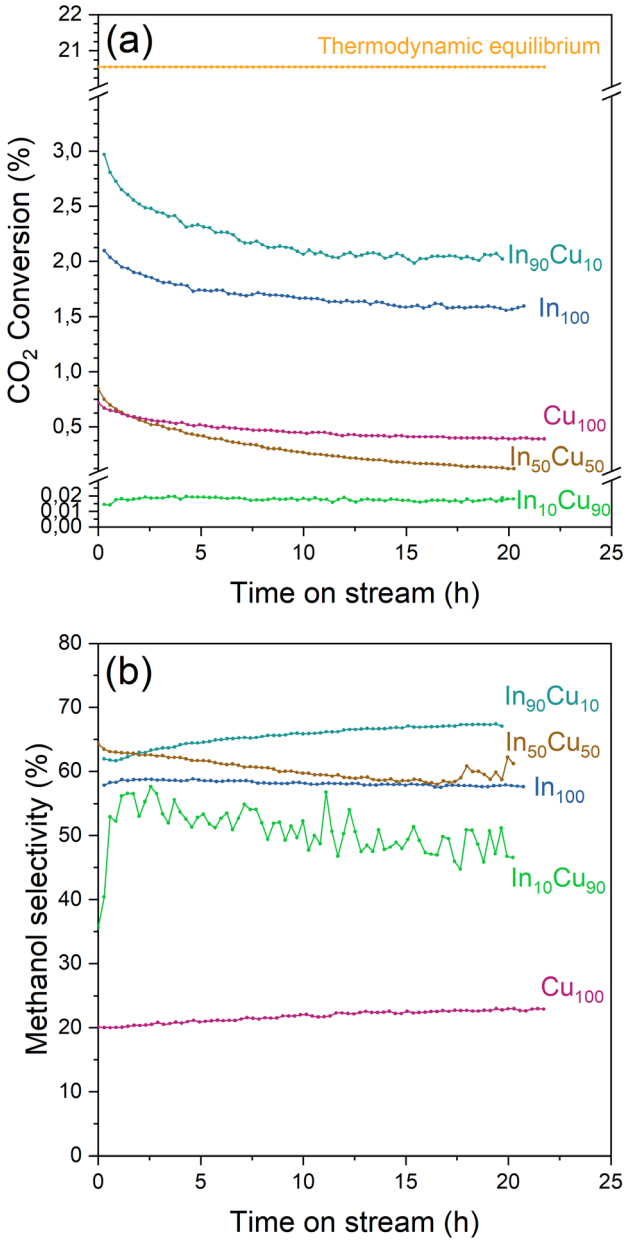

Fig. 8 (a) CO_2 conversion and (b) methanol selectivity of each catalyst during the stability test. Reaction conditions: 20 NL h^{-1} g_{cat}^{-1}, $H_2/CO_2/N_2$ = 15/5/1 molar ratio, 21 bar, 275 °C for 20 h.

best methanol selectivity after 20 h of stability test and reaches a value of 70%. It is worth noting that $In_{90}Cu_{10}$ presents a higher CO_2 conversion than In_{100} (In_2O_3). To rationalize the reason for this behaviour, these two catalysts were also investigated by means of XPS (see Fig. S12†). The superficial composition was evaluated and is reported in Table S2.† The Cu superficial concentration of the calcined $In_{90}Cu_{10}$ sample is significantly lower than the Cu bulk concentration and it increased from 1.6 at% to 2.3 at% during the reaction due to the sintering phenomena. Moreover, the evaluation of the modified Auger parameters suggests that the average oxidation state of Cu decreased from +2 to +1 while indium kept an oxidation state of +3. However, the concentration of O defects of the $In_{90}Cu_{10}$ sample increased during the TC reaction and it was higher than the concentration of O defects in the spent In_{100} TC sample. As a result, the higher performance of the $In_{90}Cu_{10}$ catalyst was ascribed both to the higher concentration of O defects and to the formation of Cu–In alloys that enhanced the CO_2 conversion and the H_2 dissociation.[20,34,36,37,46]

During the stability test, it is possible to study the deactivation phenomena. The CO_2 conversion profile for each catalyst ($In_{10}Cu_{90}$ excluded) presents a steep decline during the initial part of the tests (Fig. 8). This decrease could be caused by a loss of the active surface area due to the shrinkage and the rearrangement of the structure or by sintering of the particles that leads to a reduction of the dispersion of the active phase.[37] After this initial decrease, the deactivation phenomena continue to influence the activity with a decrease of the CO_2 conversion. In particular, the In_{100}–$In_{90}Cu_{10}$–Cu_{100} have slow activity loss after 5 h. In contrast, $In_{50}Cu_{50}$ had a very fast deactivation. Considering the information obtained from the characterizations on the fresh and spent catalysts, the deactivation phenomena that take place are sintering of the particles and deposition of carbonaceous material. In particular, the effect of sintering would seem to be more significant than the deposition of the carbonaceous material (SSA_{BET}, SEM–TEM data, TPC).

At least, the deactivation kinetic is studied with eqn (11) and (12). The best-fitting equation is (12), so the results obtained with eqn (11) are reported in Table S3.† Table 7 reports the results obtained from the interpolation of eqn (12) with experimental data. Deactivation kinetic parameters show higher deactivation rates for the $In_{50}Cu_{50}$ samples as expected from the fast CO_2 conversion reduction. Moreover, $In_{50}Cu_{50}$ and Cu_{100} catalysts show a very good fitting with our model, so it is possible to conclude that all the initial hypotheses are acceptable for these samples. Then, it is probable that sintering is the main deactivation phenomena for $In_{50}Cu_{50}$ and Cu_{100}. To further corroborate this thesis, the SSA_{BET} variation (reported in Table 7) is equal to – 89% for this sample and SEM–TEM figures (Fig. 6 for SEM images and Fig. S6† for TEM pictures) show a loss of the initial spongy structure. Instead, In_{100} and $In_{90}Cu_{10}$ show a good estimate of deactivation. The deviation from the model is caused by the initial steep decrease in approximately 5 hours. It can be concluded that sintering could be the main deactivation phenomena during the catalytic activity. Fig. 9 shows the variation of the initial conversion compared to the change of SSA_{BET} before and after the stability test. It can be observed that the catalysts which have a non-zero catalytic activity, and which do not reset to zero have a comparable specific surface area variation.

Thermocatalytic performance: activity test and kinetics. The activity tests were performed at 21 bar, flowing 20 NL h^{-1} g_{cat}^{-1} of gas mixture $H_2/CO_2/N_2$ with a molar ratio of 15/5/1. The tested temperature range was between 200 °C and 300 °C with a step of 25 °C. The activity test results are plotted in Fig. 10. The conversion increases with increasing temperature. Conversely, the selectivity towards methanol decreases with increasing temperature. Indeed, methanol is favored at low temperatures and CO is favored at high temperatures. The best point is for $In_{90}Cu_{10}$ at 300 °C that reaches a final CO_2 conversion of 4.9% and a methanol selectivity of 62.8%. In this condition, $In_{90}Cu_{10}$ (low-copper content catalyst) reaches a methanol yield equal to 51% of the equilibrium value (equilibrium

Table 7 Deactivation kinetic parameters obtained from fitting experimental data with eqn (12)

Sample	k' $Nm^3\ kg^{-1}\ h^{-1}$	Deactivation constant k_d h^{-1}	Correlation coefficient R^2 —
In_{100}	0.38	0.011	0.86
$In_{90}Cu_{10}$	0.51	0.016	0.80
$In_{50}Cu_{50}$	0.25	0.40	0.98
$In_{10}Cu_{90}$ [a]	—	—	—
Cu_{100}	0.12	0.027	0.92

[a] Catalyst with zero conversion, so the data obtained from the interpolation is meaningless and subject to physical errors.

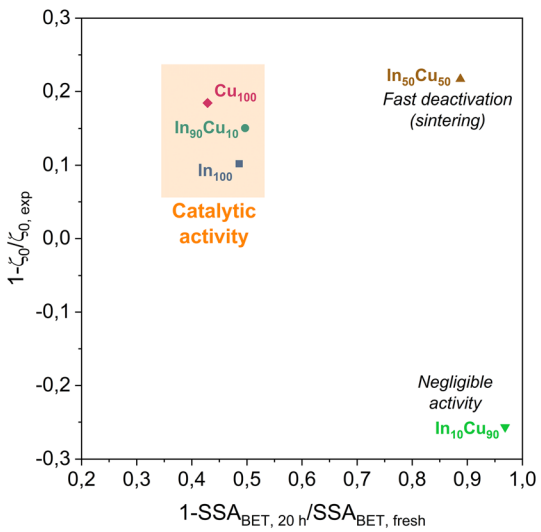

Fig. 9 Comparison between the ratio of initial conversions ζ_0 (estimated and real) and the specific surface area variation. All catalysts with significant catalytic activity are highlighted in the orange zone.

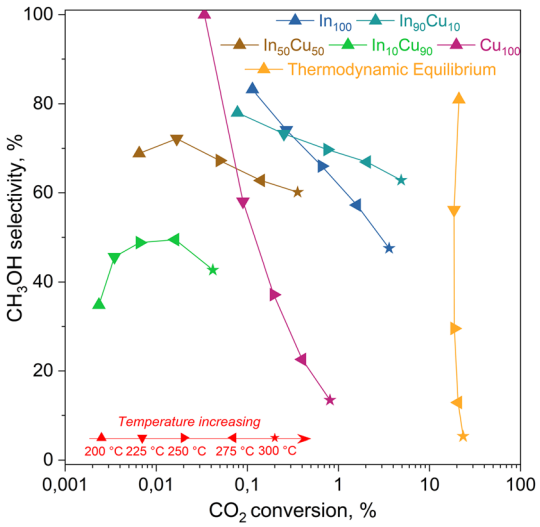

Fig. 10 Activity test results for each catalyst. On the *x*-axis, the CO_2 conversion estimated with eqn (6) and on the *y*-axis methanol selectivity calculated with eqn (7). Reaction conditions: 20 NL h^{-1} g_{cat}^{-1}, $H_2/CO_2/N_2$ = 15/5/1 molar ratio, 21 bar, 200–300 °C. The equilibrium curve was calculated as equilibrium restricted to CO and methanol.

restricted to the hydrogenation reaction of CO_2 to methanol only).

From this data, a kinetic analysis was performed. Table S4† reports the results of data fitting with eqn (14). As seen in Salomone's work,[37] the apparent activation energy is higher in CO synthesis than methanol synthesis. This is confirmed by the fact that methanol synthesis occurs at a lower temperature than the CO synthesis. In-based catalysts have similar activation energy, so the reaction mechanism of copper could be different. For this reason, an average value of E_a is fixed for the In-based catalyst in an attempt to decouple E_a and k_∞^*. Table 8 reports the apparent pre-exponential factor obtained from E_a approximation. From the obtained data, the pre-exponential factor is higher in In_{100} and $In_{90}Cu_{10}$. Therefore, it is possible to conclude that the latter catalyst has a highest number of active sites that are related to a higher concentration of O defects on the surface of the catalyst, as revealed by the XPS measurements (see Table S2†), and the interaction between In_2O_3 and Cu–In intermetallic compounds.[34,37]

Thermocatalytic performance: conclusion. Thermocatalytic tests reveal that the low-copper content catalyst has the best performance. For this reason, copper could be assumed as a good promoter for In-based catalyst. In contrast, higher amounts of copper in binary oxides catalysts give an unstable catalyst. These catalysts have a very fast deactivation or negligible activity. Finally, the Cu_{100} catalyst presents a lower catalytic activity than In_{100} and $In_{90}Cu_{10}$. The poor catalytic activity can be caused by the lack of support which would stabilize the copper. In fact, a large loss of specific surface area is observed which was already low at the outset. Concerning the alloy formation, each binary catalyst produces a specific alloy. From the literature, it is known that alloys could help the catalytic activity. Table 9 summarises the TC catalytic performance of our best catalyst (*i.e.*, $In_{90}Cu_{10}$) and compares it with other In–Cu binary oxide catalyst for CO_2 hydrogenation to methanol. It is worth noting that the $In_{90}Cu_{10}$ catalyst exhibited a high methanol productivity compared to the best TC performance of other unsupported Cu–In binary oxide catalysts (*i.e.*, CuIn-350 and CuIn (1 : 2)).

Electrocatalytic test results

The electrocatalytic tests were performed in the presence of a KOH-based solution. Indeed, although most studies have been performed with the bicarbonate anion (HCO_3^-) in an aqueous electrolyte, highly alkaline electrolytes have been shown to improve C_{2+} selectivity and suppress hydrogen evolution.[48] Besides the effect on CO_2 reduction reaction kinetics, the conductivity of the solution is an important aspect. For a large-scale implementation, the ohmic losses must be in fact minimized, given their direct impact on the energy efficiency of the whole process.[49] In this regard, the conductivity of 1.0 M KOH solution is an order of magnitude higher than in the case of 0.1 M $KHCO_3$. Therefore, the Cu-rich and In-rich catalysts were tested under such conditions to compare their performance in terms of products obtained with the same catalysts used for CO_2 thermocatalytic conditions and to literature data on heterogeneous electrocatalysts. Considering the chemical composition of the In-containing catalysts showing mainly In_2O_3 in the XRD spectra (see Fig. 3), a pre-treatment step for their partial reduction was applied to promote the formation of defective indium/indium oxide heterostructures. Indeed, the literature shows a boosted performance for CO_2 reduction due to the cooperation between formate production sites (metallic indium) and hydrogen-suppressing sites (indium oxide).[26] The electrochemical analyses were conducted under the working conditions described in the Electrode measurements section. Fig. 11(a) shows the electroactivity of the In–Cu bicomponent

Table 8 Kinetic data evaluated with a fixed E_a

	CO_2 hydrogenation			CO synthesis			CH_3OH synthesis		
Sample	E_a (kJ mol^{-1})	$\ln(k_\infty^*)$ [a]	R^2	E_a (kJ mol^{-1})	$\ln(k_\infty^*)$ [a]	R^2	E_a (kJ mol^{-1})	$\ln(k_\infty^*)$ [a]	R^2
In_{100}	87.8	27.3	0.98	103.1	29.7	1.00	80.3	25.2	0.95
$In_{90}Cu_{10}$		27.6	0.99		30.0	1.00		25.5	0.99
$In_{50}Cu_{50}$		25.0	0.99		27.4	0.99		22.8	0.99

[a] $[k_\infty^*]$ = mmol kg^{-1} h^{-1}.

Table 9 Comparison of the TC performance of Cu- and In-based binary oxide catalysts

Catalyst	Cu content at%	H_2/CO_2 ratio —	Temperature °C	Pressure bar	Space velocity NL kg_{cat}^{-1} h^{-1}	CO_2 conversion %	CH_3OH selectivity %	CH_3OH space time yield g_{CH_3OH} kg_{cat}^{-1} h^{-1}	References
$In_{90}Cu_{10}$	10.9	3/1	300	21	20 000	4.9	62.8	265	This work
CuIn-350	33.3	3/1	220	30	7500	6.9	89	131	Shi *et al.* (2019)[45]
	33.3	3/1	280	30	7500	11.4	80.5	197	
CuIn (1 : 2)	33.6	3/1	220	30	7500	7	90	131	Shi *et al.* (2022)[34]
	33.6	3/1	280	30	7500	11.5	80	192	
$CuIn@SiO_2$	8.0	3/1	280	30	7500	12.5	78.2	209	Shi *et al.* (2019)[46]
	8.0	3/1	280	30	20 000	9.8	78.1	438	
$CuIn/SiO_2$	8.0	3/1	280	30	7500	7.7	81.8	135	Shi *et al.* (2019)[46]
$Cu_1In_2Zr_4$–O	33.3	3/1	270	20	12 000	12.8	72.8	347	Gao *et al.* (2020)[47]

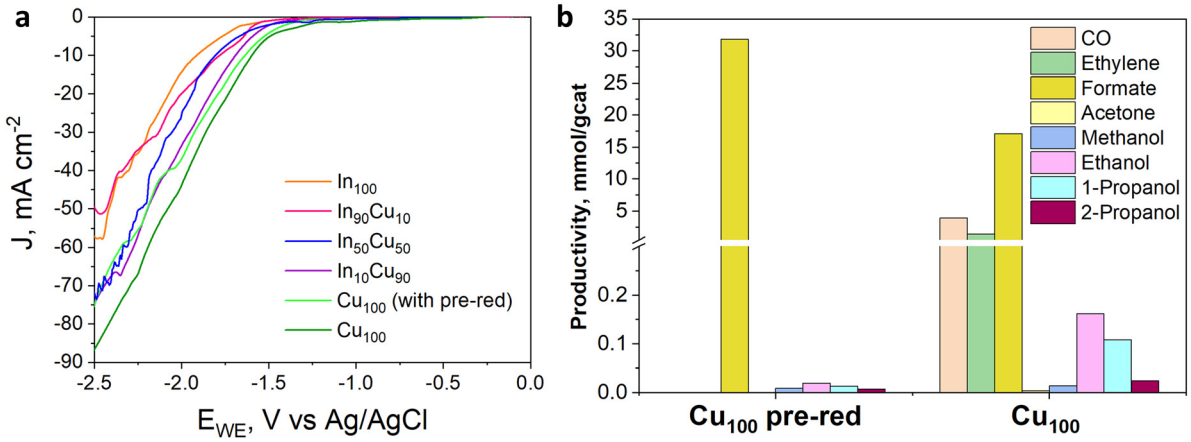

Fig. 11 (a) LSV curves under CO_2 flow of In_xCu_y-based electrodes with a catalyst loading of 1.4 mg cm^{-2} carried out in 1 M KOH aqueous electrolyte; (b) productivity of Cu_{100}-based electrodes (with and without pre-reduction treatment) with a catalyst loading of 1.4 mg cm^{-2} tested in 1 M KOH aqueous electrolyte.

catalysts between 0 and −2.5 V *vs.* Ag/AgCl in aqueous media. A rightward shift of the onset value towards more positive applied potentials can be noticed due to the Cu-enrichment. In addition, higher activity was evidenced by the In-poor catalysts: the $In_{50}Cu_{50}$, $In_{10}Cu_{90}$ and Cu_{100}, showing a cathodic current density of −75 mA cm^{-2} at −2.5 V *vs.* Ag/AgCl, which is approx. 33% higher than the one developed by In_{100} and $In_{90}Cu_{10}$ electrodes, respectively. Furthermore, to promote CO_2 conversion to more reduced products, a not pre-treated Cu_{100}-based electrode also was tested, looking to preserve the Cu^{1+}/Cu^{2+} interfaces of the fresh samples (see Fig. 3). The reductive current density recorded in this case, −85 mA cm^{-2}, at the most negative potential, far exceeded the values mentioned before.

In Fig. 11(b), from comparing the product distribution of the two Cu_{100} electrodes (the pre-reduced and the not-pre-treated one), it is possible to observe that some C-containing products other than formate were obtained by avoiding the pre-reduction step. Such a catalyst was demonstrated to also be active for the thermodynamically preferred hydrogen evolution reaction. Moreover, the distribution of gaseous and liquid CO_2 reduction products for the In_xCu_y catalysts (see Fig. 12(a)) reveals that the higher the indium content, the higher the formate faradaic efficiency (FE), suppressing the hydrogen production, as shown in Fig. 12(b). It could be attributed to the spontaneously formed oxide layer that covers the In_2O_3 materials.[50] In particular, the In_{100} catalyst reported a $FE_{formate}$ of about 16%.

With a particular focus on industrial deployment, CO_2 electrolyzers must provide modest cell voltages during operations and selectively produce concentrated target products at high rates.[51] Many researchers face this challenge by adopting a membrane-electrode assembly configuration, an attractive cell design exhibiting low ohmic loss and high energy efficiency.[52] On the other hand, the use of this kind of system for the EC CO_2R to liquid products is attractive because it could avoid problems of CO_2 solubility, and it is not required to use expensive and energy-intensive processes to recover the products from the liquid phase (such as distillation processes).[53] Moreover, MEA cells can reach current densities that are one

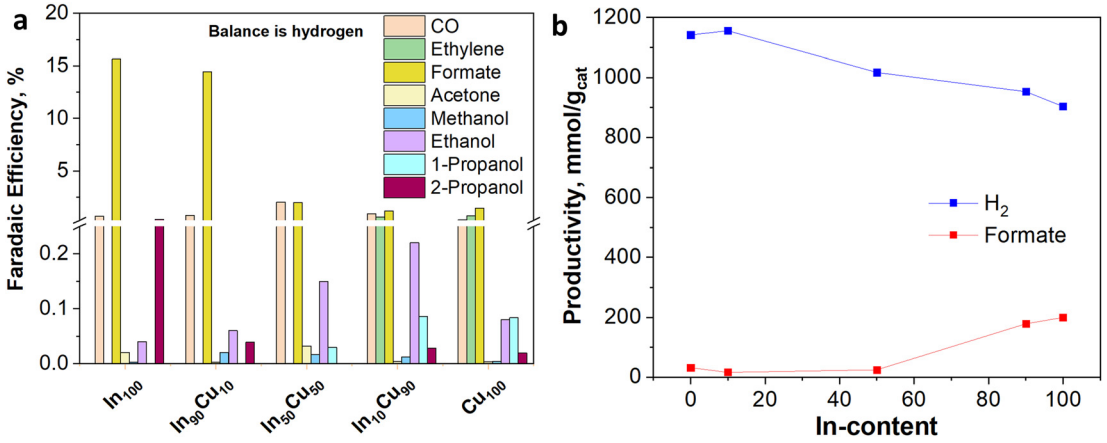

Fig. 12 (a) Faradaic efficiency distribution of In_xCu_y-based electrodes with a catalyst loading of 1.4 mg cm^{-2}, tested in 1 M KOH aqueous electrolyte at −50 mA cm^{-2} (b) relationship between hydrogen and formate productivity with the In-content.

order of magnitude higher than the ones developed with typical aqueous architectures.[54] Therefore, the MEA configuration was investigated to assess the electroactivity and selectivity of the best-performing In_xCu_y catalyst, in terms of CO_2 reduction products, under gas-phase electrolysis conditions. The linear sweep voltammetry curves characterizing the In_{100} catalyst and depicted in Fig. 13(a) revealed a lower onset potential in MEA, as well as a better total activity, with a higher cathodic current density (−65 mA cm^{-2}), attained at the highest applied potential than that observed in the GDE system. Considering the distribution of the product in Fig. 13(b), it can also be noticed that the MEA configuration improved the CO_2 reduction reaction. In particular, the MEA configuration allowed a slight increase in formate and CO productivity compared to GDE. The higher selectivity towards a single liquid demonstrates that the zero-gap electrolyzers offer a real opportunity to produce concentrated target products. Table 10 summarises the EC performance of our best electrodes ($In_{90}Cu_{10}$ and In_{100}) and compares them with other In-based catalysts for CO_2 electroreduction. Very selective and stable materials for C_1 products are reported in the literature. However, these tests have been carried out mainly in batch and small scale-systems (active area ≤ 4 cm^2). Several issues must be addressed when scaling the electrode area, among which is minimising the reactant and product gradients within the chambers, which can show up as early as in the transition from 1 cm^2 to 10 cm^2.

Electrode characterization

Post-mortem SEM and XRD analyses were conducted to get deeper insights into the electrochemical behavior of the tested electrodes. The data demonstrated the current-induced morphological and crystallographic structural changes of the indium-based catalysts occurring under different cell configurations. An EDS map (see Fig. 14) was made in the deposited layer, demonstrating a uniform coverage of In element on the carbon substrate even after the test. Other elements (*i.e.*, K, C, F, and S) were also visible in the EDS analyses due to the carbon substrate, the binder (Nafion) used for the catalytic ink preparation and the electrolyte (KOH).

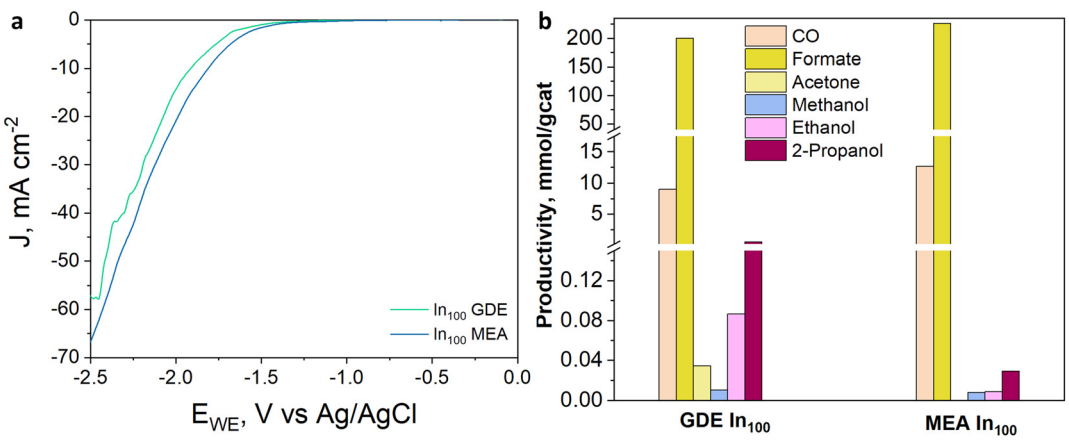

Fig. 13 (a) LSV curves under CO_2 flow and (b) productivity of In_{100}-based electrodes (GDE and MEA) with a catalyst loading of 1.4 mg cm^{-2} tested in 1 M KOH aqueous electrolyte at −50 mA cm^{-2}.

Table 10 Comparison of the EC performance of In-based catalysts

Catalyst	Cell type —	FE_{CO} %	FE_{HCOO^-} %	Current density mA cm^{-2}	Testing time hours	Area cm^2	Electrolyte Salt, concentration	References
$In_{90}Cu_{10}$	Flow cell	1	15.7	50	2	10	KOH, 1.0 M	This work
In_{100}	Flow cell	1	17.3	50	2	10	KOH, 1.0 M	This work
$ZnIn_2S_4$	Flow cell	—	97	300	60	1	$KHCO_3$, 1.0 M	Chi *et al.* 2021 [55]
In–N_3–V	H-cell	95	—	~2	14	1	$KHCO_3$, 0.5 M	Li *et al.* 2022 [56]
In–N_3–V	Flow cell	97	—	10	<1	2.25	KOH, 1.0 M	Li *et al.* 2022 [56]
In–N	Flow cell	—	91	30	3	4	KOH, 1.0 M	Zhang *et al.* 2020 [57]
In–Sn alloy	H-cell	—	78.6	~10	12	0.5	$KHCO_3$, 0.1 M	Jae Dong *et al.* 2017 [58]
$Cu_{25}In_{75}$	H-cell	—	84.1	5.3	1	—	$NaHCO_3$, 0.5 M	Zhu *et al.* 2019 [33]

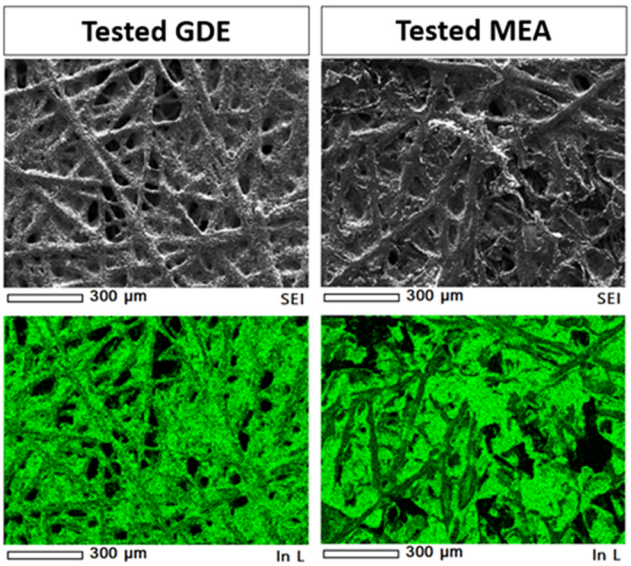

Fig. 14 SEM-EDS analyses of In_{100} electrodes: low magnification SEM images and EDS maps of In element on the GDE and MEA electrodes after electrochemical CO_2 reduction tests in 1 M KOH aqueous electrolyte at –50 mA cm^{-2}.

The *post-mortem* microscopy characterization of the In_{100} tested electrode in the GDE system demonstrated the presence of more coalesced particles than the fresh powder (Fig. 15(a)). In addition, the In_{100} tested in GDE exhibited snowflake-like particles after the electrochemical CO_2 reduction, as seen in Fig. 15(b). The test of the In_{100} catalyst in MEA configuration provoked a different morphological transformation. After testing, the pristine shape of the powder was no longer observed, having coalesced into a smooth surface covered with nanoparticles, as shown in Fig. 15(c). The chemical composition and the bonding state on the surface generated after co-electrolysis were identified by XPS analysis. Fig. S13† shows the In 3d core levels of In_{100} fresh, In_{100} tested in GDE and In_{100} tested in MEA. The binding energies at 444.1 eV and the one at 451.6 eV were assigned to In $3d_{5/2}$ and In $3d_{3/2}$, correspondingly. The spin orbit splitting between $3d_{3/2}$ and In $3d_{5/2}$ is 7.5 eV, indicating that the pristine In_{100} nanoparticles are 100% In_2O_3.[59] Moreover, it is demonstrated that In^{3+} species are stabilized at the catalyst surface of both electrodes after testing. A slight shift to higher binding energy after testing in GDE was observed, signaling that the electronic structure was affected during operation. The results are consistent with the presence of $In(OH)_3$ in the XRD patterns, confirming that the oxidation state of In^{3+} is predominant on the surface at the expense of metallic In. Interestingly the MEA electrode surface evidenced the presence of both In^{3+} and In^0. This behavior could be ascribed to the different reaction media, with aqueous electrolyte in the GDE and humidified gas in the MEA. The *post-mortem* XRD analysis of the GDE electrode detected In^0, In_2O_3, and $In(OH)_3$ phases after testing (see Fig. 15(d)). Instead, Fig. 15(e) shows that on the In_{100} tested electrode in MEA, only the $In(OH)_3$ was detected as the In-content phase. Inorganic phase related to potassium compounds were identified in both cases, which is ascribed to the electrolyte solution (either to the catholyte in the GDE case or to the anolyte in the MEA case because of K^+ crossover through the membrane).[60] The *ex situ* XRD analysis demonstrated that the presence and stabilization of $In(OH)_3$ actively participate in the electrochemical CO_2 reduction reaction mechanism, promoting the two proton-coupled electron-transfer (PCET) reactions and favouring the formation of CO and formate. Indeed, a recent study demonstrated the potential of nonreducible hydroxides to act as promoters in CO_2 reduction electrocatalysis.[32] On the other hand, the formation of other In-based species with different oxidation states than In_2O_3 (*i.e.* In and $In(OH)_3$) under the electroreductive conditions demonstrated inducing a synergistic effect that favoured the formation of C_3 products, like 2-propanol in the GDE configuration. The co-presence of those interfaces contributed to the dimerization of *CO (CO adsorbed) to generate C–C bonds, which could justify the diverse selectivity of these electrodes.

Relationships between thermo- and electrocatalysis

Indium belongs to the p-block metals, which are considered adequate in a quantitative scale of oxophilicity. The spontaneously formed oxide layer that covers the p-block metals gives them basicity, promoting the chemisorption of acidic CO_2 molecules.[61] Those point defects on the In_2O_3 surface are believed to be periodically generated, encouraging CO_2 hydrogenation to methanol and inhibiting side reactions in a ther-

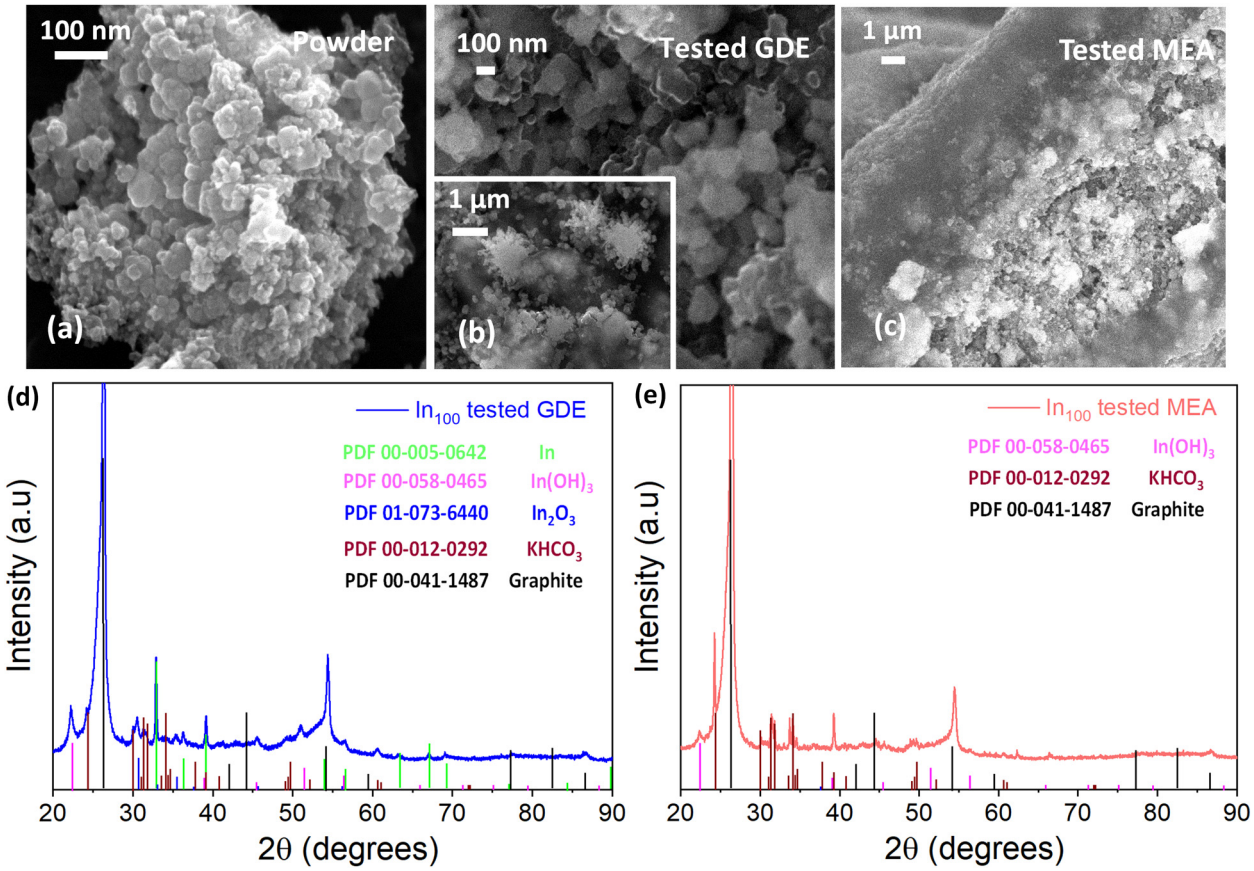

Fig. 15 In_{100} catalyst: SEM images of (a) fresh nanopowder; (b) after electrochemical CO_2 reduction in the GDE system; (c) after electrochemical CO_2 reduction in the MEA system; (d) XRD pattern obtained on the *post-mortem* GDE electrode, and (e) XRD pattern obtained at Eni SpA in the *post-mortem* MEA electrode.

mochemical system. Regarding electrocatalysis, in the literature, those post-transition elements are classified to possess a weak *H bond, suppressing hydrogen evolution and favouring the thermodynamically preferred CO_2 reduction.[62]

In situ and *operando* characterization have demonstrated that In_2O_3 is the active phase for the methanol formation, whereas In^0 led to the catalyst deactivation in the CO_2 hydrogenation at high temperatures and pressures.[62] Conversely, our results evidenced that the co-presence of different phases and oxidation states (In^0, In_2O_3, $In(OH)_3$) actively participate in the electrochemical CO_2 reduction reaction to formate and more reduced products, demonstrating that employing fundamental similarities from the viewpoint of surface science and electrical potentials instead of elevated temperatures show a synergistic interaction in hydrogenating CO_2.[32,50] Formate or formic acid is a desirable liquid fuel candidate and profitable product because of its high energy density (7.6 MJ L^{-1}) and value as a raw material for obtaining several organic compounds. At the present stage, producing formic acid or formate through two proton-coupled-electron-transfer (PCET) processes seems to have more commercial opportunities than methanol, which requires six exchanged protons and electrons to be formed.[63]

DFT calculations have been performed to establish the reaction pathways and the corresponding rate-determining steps for CO_2 hydrogenation through elevated temperatures or electrical potentials on p-block metal-based materials. Dou *et al.*[64,65] stated that exothermic methanol from CO_2 thermochemical hydrogenation could be produced through HCOO* and RWGS routes on defective In_2O_3 surfaces. The energy barrier for the formation of methanol from CO hydrogenation (1.26 eV) is lower than the formate pathway (1.54 eV), and kinetically more favourable in the presence of water-derived species.[66,67] Thus, calculations show that CO_2 hydrogenation to methanol may also follow the *COOH route, although the methoxy (H_3CO*) species obtained from formate (HCOO*) species hydrogenation are thermodynamically the most stable surface intermediates. Likewise, under electrochemical conditions, the reaction pathways for these types of electrocatalysts are similar to the abovementioned: (i) through direct carbon-bond *COOH intermediates, as described by Hori *et al.*,[68] and (ii) *via* a PCET process *via* HCOO* intermediates.[69] Our results revealed that the In_{100} is an effective In_2O_3 surface for CH_3OH formation in the thermocatalytic process, demonstrating a high selectivity (~60%). The performance was enhanced by introducing a small atomic fraction (10%) of a

d-block element (Cu) into the catalyst (~70% methanol selectivity), indicating that the energy barrier accordingly decreased. It can be attributed to preserving the oxygen vacancies on the In_2O_3 surface during the reaction (Fig. 11), stabilizing the key intermediates involved in methanol formation. On the other hand, the electrochemical CO_2 activation and hydrogenation on the In_{100} electrocatalyst faced the competitive hydrogen evolution reaction (HER), which was the major product. However, it led to formate and CO production after two PCET reactions in both GDE and MEA configurations. Interestingly, despite the potential for the spontaneous surface oxide layer, the catalyst was reduced under CO_2 reduction conditions, whose species participated in the reduction reaction. In particular, in the GDE configuration, the co-presence of In^0, In_2O_3 and $In(OH)_3$ active phases promoted *CO dimerization, leading to more reduced products, such as ethanol and 2-propanol. Nevertheless, further efforts are required to break the strong linear correlation between the free energies of COOH* and H* to boost the electrocatalytic CO_2 reduction performance over the HER, including morphology control, nanostructuring, doping, alloying and defect engineering.

Conclusions

The catalytic performance of In-based catalysts was evaluated in thermocatalytic and electrocatalytic processes. The influence of Cu-based materials was assessed in the catalyst structure. The bare Cu-based catalyst presents good CO_2 conversion but low methanol selectivity at high temperatures and pressures. Conversely, In_2O_3 shows an interesting methanol selectivity but low CO_2 conversion. Herein, the synthesized In-rich binary materials improve the methanol yield, increasing almost 3 times the productivity, achieving a value of 265 $mg_{MeOH}\ h^{-1}\ g_{In_2O_3}{}^{-1}$. Moreover, $In_{90}Cu_{10}$ showed very promising thermocatalytic performance when compared with other catalysts reported in the literature; in fact, it achieved a CO_2 conversion of 4.87%, a methanol selectivity of 62.8%, and a methanol yield of 3.06% at 300 °C, which correspond to 51% of the equilibrium methanol yield. XRD measurements after testing confirmed that the In_2O_3 phase was the active site of methanol formation during CO_2 hydrogenation. Instead, in the electrochemical process, different In active sites (In^0, In_2O_3, and $In(OH)_3$) take part in the CO_2 reduction reaction to formate and more reduced products, evidencing the potential of nonreducible hydroxides as promoters. Fundamental similarities in surface science and electrical potentials instead of elevated temperatures show a synergistic interaction in hydrogenating CO_2.

Author contributions

M. P. Mezzapesa: catalyst synthesis, thermocatalytic investigation, methodology, visualization and writing – original draft; F. Salomone: conceptualization, catalysts synthesis, thermocatalytic investigation, methodology validation and writing – original draft; H. Guzmán: conceptualization, electrocatalytic investigation, methodology validation and writing – original draft; F. Zammillo: conceptualization, electrocatalytic investigation, methodology, visualization and writing – original draft; R. Millini: conceptualization, resources, supervision and writing – review and editing; L. Bua: conceptualization, resources, supervision and writing – review and editing; G. Marra: X-ray diffraction investigation, writing – review and editing; A. Tacca: conceptualization, resources, supervision, writing – review and editing; R. Marrazzo: Raman spectroscopy investigation, visualization and writing – review and editing; N. Russo: methodology, writing – review & editing; R. Pirone: methodology, supervision and writing – review and editing; S. Bensaid: conceptualization, thermocatalytic investigation, methodology, project administration, resources, supervision and writing – review and editing; S. Hernández: conceptualization, electrocatalytic investigation, methodology, project administration, resources, supervision, writing – original draft and writing – review and editing. All authors have read and agreed to the published version of the manuscript.

Conflicts of interest

There are no conflicts to declare.

Acknowledgements

F. S. acknowledges the Italian Ministry of University and Research (MUR), program FSE REACT-EU PON Ricerca e Innovazione 2014-2020 (D.M. 1062/2021). S. H. acknowledges the project CO_2Synthesis (ID ROL: 67910) funded by Fondazione Compagnia di San Paolo in the Call Trapezio – Linea 1. This manuscript reflects only the authors' views and opinions; neither the European Union nor the European Commission can be considered responsible for them.

References

1 P. P. C. Udani, P. V. D. S. Gunawardana, H. C. Lee and D. H. Kim, Steam reforming and oxidative steam reforming of methanol over CuO-CeO_2 catalysts, *Int. J. Hydrogen Energy*, 2009, **34**, 7648–7655.
2 S. Sá, H. Silva, L. Brandão, J. M. Sousa and A. Mendes, Catalysts for methanol steam reforming-A review, *Appl. Catal., B*, 2010, **99**, 43–57.
3 Z.-J. Zuo, L. Wang, P.-D. Han and W. Huang, Insights into the reaction mechanisms of methanol decomposition, methanol oxidation and steam reforming of methanol on Cu(111): A density functional theory study, *Int. J. Hydrogen Energy*, 2014, **39**, 1664–1679.
4 J. A. Moulijn, M. Makkee and A. E. Van Diepen, *Chemical Process Technology*, 2nd edn, 2013.

5 R. C. Baliban, J. A. Elia, V. Weekman and C. A. Floudas, Process synthesis of hybrid coal, biomass, and natural gas to liquids via Fischer-Tropsch synthesis, ZSM-5 catalytic conversion, methanol synthesis, methanol-to-gasoline, and methanol-to-olefins/distillate technologies, *Comput. Chem. Eng.*, 2012, **47**, 29–56.
6 A. A. Rownaghi and J. Hedlund, Methanol to gasoline-range hydrocarbons: Influence of nanocrystal size and mesoporosity on catalytic performance and product distribution of ZSM-5, *Ind. Eng. Chem. Res.*, 2011, **50**, 11872–11878.
7 Z. Wan, W. Wu, W. Chen, H. Yang and D. Zhang, Direct synthesis of hierarchical ZSM-5 zeolite and its performance in catalyzing methanol to gasoline conversion, *Ind. Eng. Chem. Res.*, 2014, **53**, 19471–19478.
8 B. P. C. Hereijgers, F. Bleken, M. H. Nilsen, S. Svelle, K. P. Lillerud, M. Bjørgen, B. M. Weckhuysen and U. Olsbye, Product shape selectivity dominates the Methanol-to-Olefins (MTO) reaction over H-SAPO-34 catalysts, *J. Catal.*, 2009, **264**, 77–87.
9 M. R. Gogate, Methanol-to-olefins process technology: current status and future prospects, *Pet. Sci. Technol.*, 2019, **37**, 559–565.
10 M. Ye, P. Tian and Z. Liu, DMTO: A Sustainable Methanol-to-Olefins Technology, *Engineering*, 2021, **7**, 17–21.
11 P. Tian, Y. Wei, M. Ye and Z. Liu, Methanol to olefins (MTO): From fundamentals to commercialization, *ACS Catal.*, 2015, **5**, 1922–1938.
12 M. Yang, D. Fan, Y. Wei, P. Tian and Z. Liu, Recent Progress in Methanol-to-Olefins (MTO) Catalysts, *Adv. Mater.*, 2019, **31**, 1902181.
13 L. C. Grabow and M. Mavrikakis, Mechanism of methanol synthesis on cu through CO_2 and CO hydrogenation, *ACS Catal.*, 2011, **1**, 365–384.
14 R. Burch, R. J. Chappell and S. E. Golunski, Synergy between copper and zinc oxide during methanol synthesis. Transfer of activating species, *J. Chem. Soc., Faraday Trans. 1*, 1989, **85**, 3569–3578.
15 M. Bowker, R. A. Hadden, H. Houghton, J. N. K. Hyland and K. C. Waugh, The mechanism of methanol synthesis on copper/zinc oxide/alumina catalysts, *J. Catal.*, 1988, **109**, 263–273.
16 H. Guzmán, F. Salomone, E. Batuecas, T. Tommasi, N. Russo, S. Bensaid and S. Hernández, How to make sustainable CO_2 conversion to Methanol: Thermocatalytic versus electrocatalytic technology, *Chem. Eng. J.*, 2020, 127973.
17 H. Guzmán, F. Salomone, S. Bensaid, M. Castellino, N. Russo and S. Hernández, CO_2 Conversion to Alcohols over Cu/ZnO Catalysts: Prospective Synergies between Electrocatalytic and Thermocatalytic Routes, *ACS Appl. Mater. Interfaces*, 2022, **14**, 517–530.
18 C. Y. Chou and R. F. Lobo, Direct conversion of CO_2 into methanol over promoted indium oxide-based catalysts, *Appl. Catal., A*, 2019, **583**, 117144.
19 A. A. Kiss, J. J. Pragt, H. J. Vos, G. Bargeman and M. T. de Groot, Novel efficient process for methanol synthesis by CO_2 hydrogenation, *Chem. Eng. J.*, 2016, **284**, 260–269.
20 O. Martin, A. J. Martín, C. Mondelli, S. Mitchell, T. F. Segawa, R. Hauert, C. Drouilly, D. Curulla-Ferré and J. Pérez-Ramírez, Indium Oxide as a Superior Catalyst for Methanol Synthesis by CO_2 Hydrogenation, *Angew. Chem., Int. Ed.*, 2016, **55**, 6261–6265.
21 T. P. Araújo, A. Shah, C. Mondelli, J. A. Stewart, D. Curulla Ferré and J. Pérez-Ramírez, Impact of hybrid CO_2-CO feeds on methanol synthesis over In_2O_3-based catalysts, *Appl. Catal., B*, 2021, **285**, 119878.
22 J. Ye, C. Liu, D. Mei and Q. Ge, Active Oxygen Vacancy Site for Methanol Synthesis from CO_2 Hydrogenation on In_2O_3(110): A DFT Study, *ACS Catal.*, 2013, **3**, 1296–1306.
23 O. Martin, A. J. Martín, C. Mondelli, S. Mitchell, T. F. Segawa, R. Hauert, C. Drouilly, D. Curulla-Ferré and J. Pérez-Ramírez, Indium Oxide as a Superior Catalyst for Methanol Synthesis by CO_2 Hydrogenation, *Angew. Chem., Int. Ed.*, 2016, **55**, 6261–6265.
24 M. S. Frei, C. Mondelli, R. García-Muelas, K. S. Kley, B. Puértolas, N. López, O. V. Safonova, J. A. Stewart, D. Curulla Ferré and J. Pérez-Ramírez, Atomic-scale engineering of indium oxide promotion by palladium for methanol production via CO_2 hydrogenation, *Nat. Commun.*, 2019, **10**, 1–11.
25 T. Pinheiro Araújo, J. Morales-Vidal, T. Zou, R. García-Muelas, P. O. Willi, K. M. Engel, O. V. Safonova, D. Faust Akl, F. Krumeich, R. N. Grass, C. Mondelli, N. López and J. Pérez-Ramírez, Flame Spray Pyrolysis as a Synthesis Platform to Assess Metal Promotion in In_2O_3-Catalyzed CO_2 Hydrogenation, *Adv. Energy Mater.*, 2022, **12**, DOI: **10.1002/aenm.202103707**.
26 W. Yang, Y. Zhao, S. Chen, W. Ren, X. Chen, C. Jia, Z. Su, Y. Wang and C. Zhao, Defective Indium/Indium Oxide Heterostructures for Highly Selective Carbon Dioxide Electrocatalysis, *Inorg. Chem.*, 2020, **59**, 12437–12444.
27 Z. M. Detweiler, J. L. White, S. L. Bernasek and A. B. Bocarsly, Anodized Indium Metal Electrodes for Enhanced Carbon Dioxide Reduction in Aqueous Electrolyte, *Langmuir*, 2014, **30**, 7593–7600.
28 Z. Xia, M. Freeman, D. Zhang, B. Yang, L. Lei, Z. Li and Y. Hou, Highly Selective Electrochemical Conversion of CO_2 to HCOOH on Dendritic Indium Foams, *ChemElectroChem*, 2018, **5**, 253–259.
29 S. Rasul, D. H. Anjum, A. Jedidi, Y. Minenkov, L. Cavallo and K. Takanabe, A Highly Selective Copper-Indium Bimetallic Electrocatalyst for the Electrochemical Reduction of Aqueous CO_2 to CO, *Angew. Chem., Int. Ed.*, 2015, **54**, 2146–2150.
30 W. Luo, W. Xie, R. Mutschler, E. Oveisi, G. L. De Gregorio, R. Buonsanti and A. Züttel, Selective and Stable Electroreduction of CO_2 to CO at the Copper/Indium Interface, *ACS Catal.*, 2018, **8**, 6571–6581.
31 H. Xie, S. Chen, F. Ma, J. Liang, Z. Miao, T. Wang, H.-L. Wang, Y. Huang and Q. Li, Boosting Tunable Syngas Formation via Electrochemical CO_2 Reduction on Cu/In_2O_3 Core/Shell Nanoparticles, *ACS Appl. Mater. Interfaces*, 2018, **10**, 36996–37004.

32 G. O. Larrazábal, A. J. Martín, S. Mitchell, R. Hauert and J. Pérez-Ramírez, Enhanced Reduction of CO_2 to CO over Cu–In Electrocatalysts: Catalyst Evolution Is the Key, *ACS Catal.*, 2016, **6**, 6265–6274.
33 M. Zhu, P. Tian, J. Li, J. Chen, J. Xu and Y. Han, Structure-Tunable Copper–Indium Catalysts for Highly Selective CO_2 Electroreduction to CO or HCOOH, *ChemSusChem*, 2019, **12**, 3955–3959.
34 Z. Shi, M. Pan, X. Wei and D. Wu, Cu–In intermetallic compounds as highly active catalysts for CH_3OH formation from CO_2 hydrogenation, *Int. J. Energy Res.*, 2022, **46**, 1285–1298.
35 Z. Shi, Q. Tan, C. Tian, Y. Pan, X. Sun, J. Zhang and D. Wu, CO_2 hydrogenation to methanol over Cu-In intermetallic catalysts: Effect of reduction temperature, *J. Catal.*, 2019, **379**, 78–89.
36 F. Salomone, G. Bonura, F. Frusteri, M. Castellino, M. Fontana, A. M. Chiodoni, N. Russo, R. Pirone and S. Bensaid, Physico-Chemical Modifications Affecting the Activity and Stability of Cu-Based Hybrid Catalysts during the Direct Hydrogenation of Carbon Dioxide into Dimethyl-Ether, *Materials*, 2022, **15**, 7774.
37 F. Salomone, E. Sartoretti, S. Ballauri, M. Castellino, C. Novara, F. Giorgis, R. Pirone and S. Bensaid, CO_2 hydrogenation to methanol over Zr- and Ce-doped indium oxide, *Catal. Today*, 2023, **423**, 114023.
38 G. Bonura, M. Cordaro, C. Cannilla, F. Arena and F. Frusteri, The changing nature of the active site of Cu-Zn-Zr catalysts for the CO_2 hydrogenation reaction to methanol, *Appl. Catal., B*, 2014, **152–153**, 152–161.
39 O. Levenspiel, *Chemical Reaction Engineering*, John Wiley & Sons, 3rd edn, 1999, vol. 35.
40 K. S. W. Sing, Reporting physisorption data for gas/solid systems with special reference to the determination of surface area and porosity (Provisional), *Pure Appl. Chem.*, 1982, **54**, 2201–2218.
41 R. Wang, S. Sang, D. Zhu, S. Liu and K. Yu, Pore characteristics and controlling factors of the Lower Cambrian Hetang Formation shale in Northeast Jiangxi, China, *Energy Explor. Exploit.*, 2018, **36**, 43–65.
42 J. C. P. Broekhoff, *Mesopore Determination from Nitrogen Sorption Isotherms: Fundamentals, Scope, Limitations*, 1979, pp. 663–684.
43 L. Debbichi, M. C. Marco de Lucas, J. F. Pierson and P. Krüger, Vibrational Properties of CuO and Cu_4O_3 from First-Principles Calculations, and Raman and Infrared Spectroscopy, *J. Phys. Chem. C*, 2012, **116**, 10232–10237.
44 Z. Shi, M. Pan, X. Wei and D. Wu, Cu–In intermetallic compounds as highly active catalysts for CH_3OH formation from CO_2 hydrogenation, *Int. J. Energy Res.*, 2022, **46**, 1285–1298.
45 Z. Shi, Q. Tan, C. Tian, Y. Pan, X. Sun, J. Zhang and D. Wu, CO_2 hydrogenation to methanol over Cu-In intermetallic catalysts: Effect of reduction temperature, *J. Catal.*, 2019, **379**, 78–89.
46 Z. Shi, Q. Tan and D. Wu, A novel Core–Shell structured CuIn@SiO_2 catalyst for CO_2 hydrogenation to methanol, *AIChE J.*, 2019, **65**, 1047–1058.
47 J. Gao, F. Song, Y. Li, W. Cheng, H. Yuan and Q. Xu, Cu_2In Nanoalloy Enhanced Performance of Cu/ZrO_2 Catalysts for the CO_2 Hydrogenation to Methanol, *Ind. Eng. Chem. Res.*, 2020, **59**, 12331–12337.
48 T. Jaster, A. Gawel, D. Siegmund, J. Holzmann, H. Lohmann, E. Klemm and U.-P. Apfel, Electrochemical CO_2 reduction toward multicarbon alcohols – The microscopic world of catalysts & process conditions, *iScience*, 2022, **25**, 104010.
49 M. G. Kibria, J. P. Edwards, C. M. Gabardo, C. Dinh, A. Seifitokaldani, D. Sinton and E. H. Sargent, Electrochemical CO_2 Reduction into Chemical Feedstocks: From Mechanistic Electrocatalysis Models to System Design, *Adv. Mater.*, 2019, **31**, 1807166.
50 B. Jia, Z. Chen, C. Li, Z. Li, X. Zhou, T. Wang, W. Yang, L. Sun and B. Zhang, Indium Cyanamide for Industrial-Grade CO_2 Electroreduction to Formic Acid, *J. Am. Chem. Soc.*, 2023, **145**, 14101–14111.
51 C. M. Gabardo, C. P. O'Brien, J. P. Edwards, C. McCallum, Y. Xu, C. T. Dinh, J. Li, E. H. Sargent and D. Sinton, Continuous Carbon Dioxide Electroreduction to Concentrated Multi-carbon Products Using a Membrane Electrode Assembly, *Joule*, 2019, **3**, 2777–2791.
52 L. C. Weng, A. T. Bell and A. Z. Weber, Towards membrane-electrode assembly systems for CO_2 reduction: A modeling study, *Energy Environ. Sci.*, 2019, **12**, 1950–1968.
53 H. Guzmán, N. Russo and S. Hernández, CO_2 valorisation towards alcohols by Cu-based electrocatalysts: challenges and perspectives, *Green Chem.*, 2021, **23**, 1896–1920.
54 L. Ge, H. Rabiee, M. Li, S. Subramanian, Y. Zheng, J. H. Lee, T. Burdyny and H. Wang, Electrochemical CO_2 reduction in membrane-electrode assemblies, *Chem*, 2022, **8**, 663–692.
55 L.-P. Chi, Z.-Z. Niu, X.-L. Zhang, P.-P. Yang, J. Liao, F.-Y. Gao, Z.-Z. Wu, K.-B. Tang and M.-R. Gao, Stabilizing indium sulfide for CO_2 electroreduction to formate at high rate by zinc incorporation, *Nat. Commun.*, 2021, **12**, 5835.
56 S. Li, X. Lu, S. Zhao, M. Ceccato, X.-M. Hu, A. Roldan, M. Liu and K. Daasbjerg, p-Block Indium Single-Atom Catalyst with Low-Coordinated In–N Motif for Enhanced Electrochemical CO_2 Reduction, *ACS Catal.*, 2022, **12**, 7386–7395.
57 A. Zhang, Y. Liang, H. Li, B. Zhang, Z. Liu, Q. Chang, H. Zhang, C.-F. Zhu, Z. Geng, W. Zhu and J. Zeng, In-Situ Surface Reconstruction of InN Nanosheets for Efficient CO_2 Electroreduction into Formate, *Nano Lett.*, 2020, **20**, 8229–8235.
58 W. J. Dong, C. J. Yoo and J.-L. Lee, Monolithic Nanoporous In–Sn Alloy for Electrochemical Reduction of Carbon Dioxide, *ACS Appl. Mater. Interfaces*, 2017, **9**, 43575–43582.
59 X. Zuo, Z. Yang, J. Kong, Z. Han, J. Zhang, X. Meng, S. Hao, L. Wu, S. Wu, J. Liu, Z. Wang and F. Wang, Imbedding Pd Nanoparticles into Porous In_2O_3 Structure for Enhanced

Low-Concentration Methane Sensing, *Sensors*, 2023, **23**, 1163.

60 G. A. El-Nagar, F. Haun, S. Gupta, S. Stojkovikj and M. T. Mayer, Unintended cation crossover influences CO_2 reduction selectivity in Cu-based zero-gap electrolysers, *Nat. Commun.*, 2023, **14**, 2062.

61 Z. Yang, F. E. Oropeza and K. H. L. Zhang, P-block metal-based (Sn, In, Bi, Pb) electrocatalysts for selective reduction of CO_2 to formate, *APL Mater.*, 2020, **8**, 060901.

62 D. Cai, Y. Cai, K. B. Tan and G. Zhan, Recent Advances of Indium Oxide-Based Catalysts for CO_2 Hydrogenation to Methanol: Experimental and Theoretical, *Materials*, 2023, **16**, 2803.

63 L. Ai, S. Ng and W. Ong, A Prospective Life Cycle Assessment of Electrochemical CO_2 Reduction to Selective Formic Acid and Ethylene, *ChemSusChem*, 2022, **15**(19), e202200857.

64 M. Dou, M. Zhang, Y. Chen and Y. Yu, DFT study of In_2O_3-Catalyzed methanol synthesis from CO_2 and CO hydrogenation on the defective site, *New J. Chem.*, 2018, **42**, 3293–3300.

65 M. Dou, M. Zhang, Y. Chen and Y. Yu, Theoretical study of methanol synthesis from CO_2 and CO hydrogenation on the surface of ZrO_2 supported In_2O_3 catalyst, *Surf. Sci.*, 2018, **672–673**, 7–12.

66 S. Dang, B. Qin, Y. Yang, H. Wang, J. Cai, Y. Han, S. Li, P. Gao and Y. Sun, Rationally designed indium oxide catalysts for CO_2 hydrogenation to methanol with high activity and selectivity, *Sci. Adv.*, 2020, **6**(25), eaaz2060.

67 Y.-F. Zhao, Y. Yang, C. Mims, C. H. F. Peden, J. Li and D. Mei, Insight into methanol synthesis from CO_2 hydrogenation on Cu(111): Complex reaction network and the effects of H_2O, *J. Catal.*, 2011, **281**, 199–211.

68 Y. Hori, H. Wakebe, T. Tsukamoto and O. Koga, Electrocatalytic process of CO selectivity in electrochemical reduction of CO_2 at metal electrodes in aqueous media, *Electrochim. Acta*, 1994, **39**, 1833–1839.

69 J. S. Yoo, R. Christensen, T. Vegge, J. K. Nørskov and F. Studt, Theoretical Insight into the Trends that Guide the Electrochemical Reduction of Carbon Dioxide to Formic Acid, *ChemSusChem*, 2016, **9**, 358–363.

